

# **Energy Harvester Design for Intelligent Tyre Systems**

**Otso Jousimaa**

**School of Electrical Engineering**

Thesis submitted for examination for the degree of Master of  
Science in Technology.

Esbo XX.XX.XXXX

**Thesis supervisor:**

Prof. Arto Visala

**Thesis advisors:**

M.Sc. Yi Xiong

D.Sc. (Tech.) Ari Tuononen

Author: Otso Jousimaa		
Title: Energy Harvester Design for Intelligent Tyre Systems		
Date: XX.XX.XXXX	Language: English	Number of pages: 7+62
Department of Automation and Systems Technology		
Professorship: Smart products		
Supervisor: Prof. Arto Visala		
Advisors: M.Sc. Yi Xiong, D.Sc. (Tech.) Ari Tuononen		
<p>Modern tyres have sensor systems which require energy. Currently these systems are powered by batteries, but changing batteries is cumbersome. Harvesting electrical energy from tyre movement and deformation was experimented with piezoelectric and electromagnetic harvester design. Harvested power was rectified and stored into supercapacitor at voltage level usable by modern microcontrollers. Tens of milliwatts of electrical power was obtained from both harvesters in a vibration exciter test setup, and piezoelectric harvester produced 50 microwatts of electrical power chassis dynamometer test rig.</p>		
Keywords: Energy harvesting, tyre sensors		

Tekijä: Otso Jousimaa		
Työn nimi: Energy Harvester Design for Intelligent Tire Systems		
Päivämäärä: XX.XX.XXXX	Kieli: Englanti	Sivumäärä: 7+62
Automaatio- ja systeemiteknikan laitos		
Professuuri: Älykkääät tuotteet		
Työn valvoja: Prof. Arto Visala		
Työn ohjaajat: DI Yi Xiong, TkT Ari Tuononen		
Moderneissa renkaissa on anturijärjestelmiä jotka tarvitsevat energiaa. Nykyään nämä järjestelmät saavat tehonsa patterista, mutta pattereiden vaihtaminen on työlästä. Energian harvestointia renkaan liikkeestä ja muodonmuutoksista kokeiltiin pietsosähköisellä ja sähkömagneettisella harvesterilla. Harvestoitu energia tasasuuunnattiin ja varastoitiin superkapasitoriin moderneille mikrokontrollereille soveltuvalla jännitetasolla. Tärinägeneraattorilla harvestereista saavutettiin kymmenien milliwattien sähköteho, ja pietsosähköinen kerän tuotti 50 mikrowattia tehoa dynamometritestialustalla.		
Avainsanat: Energian harvestointi, rangasanturit		

## Preface

This research was carried out in the Laboratory of Vehicle Technology, Aalto University School of Engineering during 2015-2016. Some sections of the work relating to piezoelectric harvester and electronics design have been used as a basis for IEEE Intelligent Vehicles Symposium 2016 conference paper pending peer review.

I am deeply grateful for my thesis instructors M.Sc Yi Xiong and D.Sc Ari Tuononen for their encouragement, guidance and patience in all phases of the work. Special thanks go to my supervisor Prof. Arto Visala for his confidence in me and my supervisors during the work.

I would like to express my gratitude to Daniel Edwards, Lauri Jämsä, Gaja Kochaniewicz, Martti Paalanen, Ivan Raul, Markku Rouvala and Heikki Salminen for providing insights in use cases, manufacturing methods, soundness of various ideas and textual clarity for the work.

The work was financially supported by Henry Ford Säätiö

Otaniemi, XX.XX.XXXX

Otso J. Jousimaa

# Contents

<b>Abstract</b>	ii
<b>Abstract (in Finnish)</b>	iii
<b>Preface</b>	iv
<b>Contents</b>	v
<b>Symbols and abbreviations</b>	vii
<b>1 Introduction</b>	1
1.1 Energy harvesting . . . . .	2
1.1.1 Overview of methods . . . . .	2
1.1.2 Resonance-based piezoelectric harvesting . . . . .	3
1.1.3 Impact-based piezoelectric harvesting . . . . .	4
1.1.4 Electromagnetic harvesting . . . . .	5
1.2 Structure of a tyre . . . . .	7
1.3 Environment inside tyre . . . . .	8
<b>2 Design</b>	11
2.1 System-level design . . . . .	11
2.2 Power requirements of a system . . . . .	12
2.3 Electromagnetic harvester design . . . . .	13
2.3.1 Basics of electromagnetical vibration harvester . . . . .	13
2.3.2 Analytical model of electromagnetical vibration harvester . . . . .	15
2.3.3 Experimental and FEA modeling of electromagnetic harvester	20
2.3.4 Mechanical design of electromagnetic harvester . . . . .	22
2.4 Piezoelectric harvester design . . . . .	23
2.4.1 Basics of piezoelectric energy harvesting . . . . .	23
2.5 Electronic design . . . . .	26
2.5.1 Simulation of circuit . . . . .	26
2.5.2 Schematic design . . . . .	27
2.5.3 Circuit layout . . . . .	33
2.6 Mechanical design of harvester . . . . .	35
<b>3 Results and discussion</b>	37
3.1 Experimental results of electromagnetic harvester . . . . .	37
3.1.1 Test setup . . . . .	37
3.1.2 Frequency domain results . . . . .	38
3.1.3 Time domain results . . . . .	39
3.2 Experimental results of piezoelectric harvester . . . . .	45
3.2.1 Frequency domain results . . . . .	45
3.2.2 Time domain results . . . . .	46
3.3 Harvesting circuit results . . . . .	49

3.3.1	Revisited circuit design . . . . .	49
3.3.2	Measuring supercapacitor parameters . . . . .	52
3.4	Performance inside tyre . . . . .	54
3.5	Comparison to state-of-art results . . . . .	55
<b>4</b>	<b>Conclusions</b>	<b>57</b>
<b>References</b>		<b>58</b>

# Symbols and abbreviations

## Symbols

<b>A</b>	area
<b>B</b>	magnetic flux density
<i>c</i>	speed of light in vacuum $\approx 3 \times 10^8$ [m/s]
$\varepsilon$	electromotive force
<b>F</b>	mechanical force
<b>I</b>	electrical current
<b>l</b>	length
$\Phi_B$	magnetic flux through loop area
$\rho$	resistivity
<b>P</b>	power
<b>p</b>	pressure
<b>U</b>	input to system
<b>V</b>	voltage
<b>Y</b>	output from system
<b>Z</b>	complex impedance

## Operators

$\frac{d}{dt}$	derivative with respect to variable <i>t</i>
$\frac{\partial}{\partial t}$	partial derivative with respect to variable <i>t</i>
$\sum_i$	sum over index <i>i</i>

## Abbreviations

AC	Alternating Current
BLE	Bluetooth Low Energy
DC	Direct Current
EMF	Electromotive Force
IC	Integrated Circuit
MEMS	Microelectromechanical Systems
MPPT	Maximum Power Point Tracking
PV	Photovoltaic
RF	Radio Frequency
SMPS	Switch-Mode Power Supply
TPMS	Tire Pressure Monitoring Sensors

# 1 Introduction

As technology advances, it has become possible to build small, light-weight and yet powerful sensor platforms which can communicate wirelessly with their environment. New kind of applications are being created using the possibilities given by these sensor platforms. A common feature with all of these devices is that they need power to function, even if the power needed is minuscule.

Traditionally wireless devices have been powered by batteries, but as the number of sensors increases, the cost of changing or charging batteries becomes significant part of cost of any system. This is especially relevant for the devices which are in hard-to-reach areas, such as inner parts of heavy machinery, walls of bridges and high rise buildings, remote environmental sensors et cetera. On some applications the life of the battery can become a limiting factor for the lifetime of entire sensor, if cost of installing new sensor is similar to cost of replacing the battery.

A new approach to powering the device is to harvest the energy from it's surroundings using ambient energy as the power source. Examples of such energy sources are solar, wind, temperature differentials, and vibration. The technology to utilise some of these power sources, such as wind and solar is already widely deployed and even used in the large-scale power production. On a smaller scale the demand for reliable and efficient solutions has been growing strongly with the advent of wireless low-power devices and a lot of research has focused on creating suitable technologies and devices for low-power energy harvesting.

This work focuses on powering one of such devices, namely a sensor inside a car tyre. The car tyre provides some unique challenges and opportunities, as there is a lot of energy available, but on the other hand operating conditions can be extremely harsh with large temperature ranges and extreme vibration and shocks especially in rougher road conditions.

Car tyre sensing itself has been in focus of a lot development lately, as legislation in the United States demands new tyres being fitted with a pressure sensor to warn drivers about the low pressure and related higher fuel consumption, wear on tyre and even elevated risk of accidents. European Union has also laws which require Tire Pressure Monitoring Sensors (TPMS) on new passenger cars.

This paper is based on my Master's Thesis which is still a work in progress. The next section has overview of car tyres and the operational environment inside them. A quick review on possible energy harvesting technologies is made, piezoelectric and electromagnetic energy harvesting are selected for in depth comparison. Two different approaches are used determining the applicability of energy harvesting method: electromagnetic generator is researched based on theoretical analysis and simulation while piezoelectric harvesting is researched using experimental methods.

Conclusion presents findings based on the theoretical and experimental research phases of the work and discusses future work to be done to validate findings of theoretic designs.

## 1.1 Energy harvesting

### 1.1.1 Overview of methods

First step of designing a system for energy harvesting was to identify the currently known methods and their properties. Kubba et al. [1] have done a study on tyre pressure sensor technology, they present electromagnetic, electrostatic, piezoelectric and thermal solutions as possible candidates for energy harvesting. In addition, triboelectric and magnetostrictive methods have been proposed by Bowen et al [2]. Outside of the context of tyres, Paradiso et al. [3] present solar and radiowave harvesting techniques. Radioactive power source has been suggested by Lal et al [4].

Electromagnetic power sources are based on Faraday's law of electromagnetic induction. A magnet and a coil are put in motion relative to each other, and the changing magnetic flux through the coils of the generator produces voltage. Current through such device is determined by load resistance. Technology is widely used in power generation, where a primary power source such as wind or flow of water provides rotation for the generator. While conventional designs use rotational movement, linear generator designs exist. Boldea and Nasar [5] provide an overview of linear generator and actuator theory.

Electrostatic devices charge plates of a capacitor and use mechanical vibration to vary the structure of the capacitor. As the capacitance value changes with the structure, energy can be harvested from increased potential energy in capacitor. Drawback of this method is the required control electronics and high polarisation voltages needed for maximal efficiency. There are also electrostatic methods which use electrets. These electrets hold constant charge and polarisation for years and they can be used in electrostatic harvesters which do not require an external excitation source [6]. As electret elements and electrostatic generators are not readily available, they have been excluded from this study.

Piezoelectric materials generate charge in response of mechanical stress. This stress can be caused by firmly attaching the piezoelectric element to a surface which deforms (simply supported) or by leaving one end of the element free-hanging while other end is fixed (cantilevered). Dynamics of the generator are very different for the different configurations, Kim et al. [7] provides a model for impact-based piezoelectric harvester while Erturk et al. have done in-depth analysis of cantilevered piezoelectric modelling [8].

Thermal solutions can be further divided into subcategories. Seebeck-effect where a temperature gradient in a semiconductor material causes voltage between poles of the material is widely used in temperature sensing, but to generate appreciable amounts of power large temperature gradients of over hundred °C are required according to study by Amatya et al. [9]. Such temperature gradients are not practical inside the tyre. Pyroelectric materials do not require differential of temperature, they generate energy when the temperature of the entire element changes [10]. As the temperature inside tyre remains rather constant over long periods of time, these methods are not practical for this application.

Triboelectricity generates power using friction between two materials, a classic example of this is Benjamin Franklin's experiments on charging various rods by

rubbing them against different materials. A flexible triboelectric generator has been presented by Fan et al. [11]. Triboelectric sheets are not readily available and their construction is complex, so triboelectric generation is excluded from this work.

Magnetostrictive materials change their magnetic field in response to external mechanical stress. This change can be utilised to create a magnetic flux through coils as in electromagnetic generators. A magnetostrictive generator was built by Wang et al. [12].

Solar energy can be harvested by using sun as a energy source for a thermal energy harvesting or by utilising the photovoltaic (PV) effect to generate electricity from photons hitting PV material. PV technology is mature and widely used, and PV cells attached to rim of tyre could produce ample power during summertime. PV cells would however incur extra maintenance as the rims would have to be cleaned whenever power output falls.

Radio wave harvesting uses antennas to collect energy from ambient radio transmissions, such as WiFi- and cellular signals. Patel et al [13] have built a demonstration device which uses TV broadcasts as an energy source. The tyre material dampens any Radio frequency (RF) broadcasts, which makes RF energy harvesting poorly suited for the application.

Radioactive energy harvesting resembles battery or fuel cell. A radioactive material is deposited in generator near piezoelectric cantilever. Radioactive decay charges proof mass of piezoelectric cantilever until the proof mass contacts the radioactive material by electrostatic attraction, at which point the electrical charge is balanced and piezoelectric beam begins resonant vibration as in normal piezoelectric harvesting. Such a battery has lifetime limited only by half-life of the used material. Lal and Blanchard [4] present such a battery. This kind of battery would be redundant for the application, as there already exists energy in rotation of tyre which can be used to energise the cantilever.

In conclusion, a wide range of energy harvesting technologies have been identified. As their primary properties are known, we can narrow down the suitable technologies to electromagnetic and piezoelectric. These technologies are studied further to identify optimal choice for the application.

### 1.1.2 Resonance-based piezoelectric harvesting

Piezoelectric materials produce voltage in response to mechanical stress. The effect is bidirectional, piezoelectric element can also produce mechanical strain in response to applied voltage. The material has crystalline structure with electrical dipoles in balanced state when no stress is applied. Mechanical stress unbalances these dipoles, creating element which electronically resembles a charged capacitor.

A common approach to piezoelectric harvesting is to configure the element as a cantilever and tune the resonant frequency of the system to dominant frequency of the surrounding environment. This kind of system is shown in figure 1. In some applications, such as in machines running at the frequency of power grid (50 Hz or 60 Hz) this kind of frequency-tuning is relatively straightforward.

This kind of resonant harvesting is challenging in tyre. The energy harvester



Figure 1: Piezoelectric generator configured as cantilever by Arroyo et al [14].

has a very sharp peak efficiency frequencies, and dominant frequency of tyre varies with the speed of car. On the other hand, there is almost guaranteed broadband energy available from moments where tyre contacts road. There is also some research on tuning the resonant frequency of cantilevered piezoelectric harvester by Singh et al [15]. They used intelligently driven Switch-Mode Power Supply (SMPS) to impedance-match the load to piezoelectric element. As the electro-mechanical nature of piezo means changing load changes the mechanical properties of element, resonance frequency can track the dominant frequency of system within some limits. Figure 2 shows the tracking behaviour Singh et al achieved, resonance can be adjusted in range of 65 - 70 Hz.

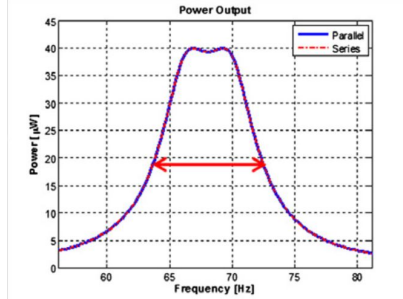


Figure 2: Frequency tuning results by Singh et al [15].

The results of Singh et al. can be considered as the state-of-art for resonance-based piezoelectric harvesting in tyre, and their power output was around  $40\mu\text{W}$  at peak efficiency. Therefore other methods have to be explored for energy harvester design.

### 1.1.3 Impact-based piezoelectric harvesting

As the resonant harvesting is not feasible in the environment inside tyre, another method would be to use an impactor to hit a piezoelectric plate on every cycle of a tyre. These impacts would provide energy once per rotation of a tyre. This method has been tried before by Manla et al [16]. Their generator produced 4 mW electrical power.

As 4mW is plenty in field of low-power electronics, this approach deserves an in-depth study. Piezoelectric elements are often electrically modelled as current source with parallel capacitor or voltage source with series capacitor, as shown in figure 3 by Kanda et al [17]. There are also a lot more complex models which account for mechanical phenomena in piezo, as well as loading effects coupling on mechanical model. For the purposes of model identification for the piezo only simplest voltage source (a) and current source (b) models are explored.

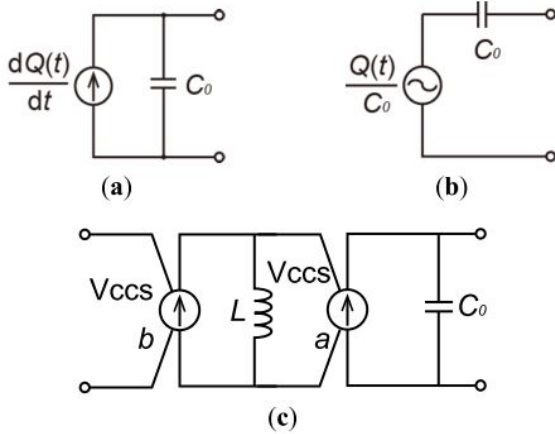


Figure 3: Electrical equivalent models for piezoelectric element [17].

The model (b) of figure 3 shows clearly that no DC current can flow in or out of piezo element. Maximum current in any cycle of piezo is limited by the open loop voltage which is seen on the terminals of piezo and the piezo capacitance in series.

The implication for impact-based harvesting is somewhat discouraging: total amount of power obtainable is limited by the frequency of impacts. However, if there is any natural resonance frequency for the piezo generator, some of the energy in impact should be in appropriate spectrum for the generator and the generator could produce decaying amount of power in-between of impacts.

#### 1.1.4 Electromagnetic harvesting

Electromagnetic harvesting is based on Faraday's law of induction: A loop of wire acquires electromotive force (EMF) in response to a changing magnetic field. More formally:

$$\varepsilon = -\frac{d\Phi_B}{dt}, \quad (1)$$

where  $\varepsilon$  is the EMF,  $\Phi_B$  is magnetic flux through loop area, and  $t$  is time. Negative sign signifies that emf opposes the change of magnetic flux. For a tightly wound coil of wire, the equation can be stated as:

$$\varepsilon = -N_{turns} \frac{d\Phi_B}{dt}, \quad (2)$$

where  $N_{turns}$  is the number of turns in a coil. [18, p.999]

It's important to notice that magnetic flux through wire  $\Phi_B$  can change for a variety of reasons: the source of field can be in motion, strength of field can vary, the coil can be in motion, and the shape of coil can vary. In an energy harvesting application in an environment with vibrations motional energy is readily available, so we focus on energy harvesting methods which either move the source of magnetic field or the coil itself.

It can be determined from equation (2) that the energy available increases with the strength of magnetic source, number of turns in a coil and rate of change in the magnetic field.

Magnetic source can be either a permanent magnet or an electrically induced source as in induction motors. Induction-based generators require reactive power to start up, which means that any harvester design incorporating an induction generator would need a secondary power source to start the inductive generator. Hence the focus of this thesis will be in permanent magnet designs.

In addition to voltage available from the generator, it's important to consider the source impedance. A very simple electrical equivalent model of the generator is presented in figure 4, where generator is presented as a voltage source in series with lumped inductor and resistor [19].

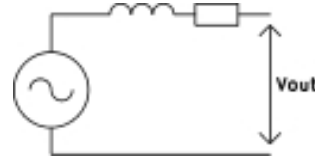


Figure 4: A simple electromechanical generator equivalent circuit.

This model is greatly simplified and it does not account for factors such as effect of electromagnetic force on mechanical structure of the generator. Even with these limitations, the model is still useful as it can be used to determine an optimal load for the generator.

The power output can be written formally as:

$$P_{generated}(s) = \varepsilon(s) * I_{generated}(s), \quad (3)$$

where  $P_{generated}(s)$ ,  $\varepsilon(s)$ ,  $I_{generated}(s)$  are complex frequency-domain power, voltage and current dependent. Voltage is determined by EMF as described above. Current can be written as:

$$I_{generated}(s) = \frac{\varepsilon(s)}{Z_{generator}(s) + Z_{load}(s)}, \quad (4)$$

where  $Z_{generator}(s)$  and  $Z_{load}(s)$  are complex impedance of load and generator. This equation is valid only for linear systems, so for example rectifying and converting

power with switch-mode power supply (SMPS) reduces accuracy of the equation. Substituting (4) into (3) we obtain:

$$P_{generated}(s) = \varepsilon(s) * \frac{\varepsilon(s)}{Z_{generator}(s) + Z_{load}(s)}. \quad (5)$$

Total power into load can be written as:

$$P_{load}(s) = \varepsilon(s) * \frac{Z_{load}(s)}{Z_{generator}(s) + Z_{load}(s)} * \frac{\varepsilon(s)}{Z_{generator}(s) + Z_{load}(s)}. \quad (6)$$

It's easy to see from (6) that if the load impedance is infinite or zero, there is no power generated. It can be shown that maximum power is generated when load impedance is complex conjugate of generator impedance,  $Z_{generator}(s) = Z_{load}(s)^*$ . Another consideration is efficiency of the generator: the electrical efficiency is defined as ratio of power flowing into load and total power generated. Equation (6) can be used to show that when load impedance is equal to generator impedance, efficiency is 50%. Efficiency rises with the load impedance, which is why generators are rarely run at their maximum power. In our application the harvested power is minuscule compared to power available in tyre, so it makes sense to try to match the load impedance for maximum power.

In an energy harvesting application it is important to consider the validity of established theory when generator is scaled to centimetres or even smaller dimensions. Many assumptions, such as coil being tightly wound and made of thin wire might become invalid at microscale. O'Donnell et al. [20] have done a study on the effects of scaling dimensions downwards down to millimetre range, and they concluded that power available from generator is proportional to fourth power of generator dimension for cubical generators. Another of their primary findings was that a microfabricated generator becomes more effective than a traditional wire-wound generator when design is scaled below 2mm length or in 8mm<sup>3</sup> volume. It can be concluded that in this application it is reasonable to use a wire-wound generator over microfabricated one, as the generator dimensions can be an order of magnitude larger than this crossover point.

## 1.2 Structure of a tyre

Tyres are composed of several layers with different functions. Figure 5 by Gent et al. [21] shows the layered structure. From outer tread to inner lining, the layers are:

**Tread** provides traction for driving, braking and cornering. Pattern and materials on tread is a compromise between wear resistance, traction, handling and rolling resistance

**Belts** provide mechanical strength, impact resistance and keep tyre from expanding under centrifugal forces.

**Body ply** provides strength to contain the air pressure.

**Innerliner** is a compound specifically designed to improve air retention in tyre.

In addition there are layers designed to improve tyre reliability, such as the belt wedge which reduces shear between belts.



Figure 5: Structure of a tyre [21].

In endurance testing of tyres the car is driven at test track in three shifts until desired number of course driving kilometres have been reached. In outdoor testing each company has their own proprietary test protocol. Indoor testing has standards, which mandates pressure, ambient temperature and speed as well as time driven. According to Gent et al. [21] this indoor testing takes 34 hours of driving at 120 km/h.

In addition to endurance testing, there is high-speed testing where tyre speed is gradually accelerated in steps of 10 km/h at regular intervals until target speed is reached. Energy harvester should survive these tests to be considered a viable design for road conditions.

### 1.3 Environment inside tyre

The energy harvester will be placed inside the tyre. Previous studies by Niskanen et al [22]. have shown that the tyre will experience acceleration in all three axes. Tangential and centripetal accelerations are dominant, they can reach amplitudes up to 150 g in test fixture. In addition a study done by Löhndorf et al. [23] shows shock survival of up to 4 000 - 5 000 g is required for reliability.

Temperature inside of the tyre will reach equilibrium in ambient + 5-10 °C, so operation temperature should be in range of -40 to + 75 °C to have some safety margin on top of usual ambient conditions.

Previous work by Niskanen et al. [22] was used to as a basis for analysis of characteristics of acceleration inside the tyre. Raw data was used to gather minimum and maximum values of acceleration as well as frequency components inside tyre. Data was gathered at 20 km/h, 60 km/h and 80 km/h speeds. Figure 7 shows time domain representations of the acceleration along 3 axes as shown in figure 6.

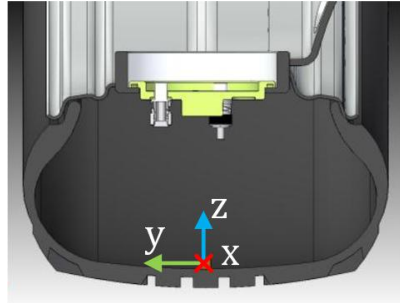


Figure 6: Axes in measurement by Matilainen et al. [24]

Frequency domain representations were calculated in Matlab. There are two main contributors to base frequencies: first is the rotational frequency of tyre itself and second is the impact when the tyre deforms as it contacts the drum.. There is clearly visible series of frequency components spaced at the rotational frequency of tyre as well as shock harmonics at upper frequencies. Figure 8 shows the total frequency spectrum and the dominant frequency components.

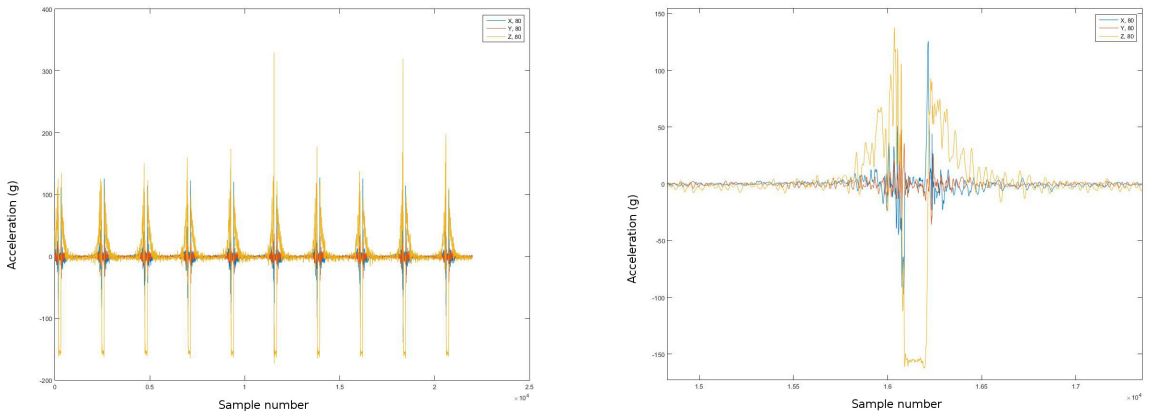


Figure 7: Acceleration of inner lining of tyre at 80 km/h in time domain.

It's important to notice that the sensor used was piezoelectric, which forms a highpass filter as the operation of sensor is based on charge between layers. This charge dissipates over time, so the steady-state centripetal acceleration reads as zero. Any device on the rotating tyre will experience centripetal acceleration (acceleration toward centre of rotation) at the amplitude of:

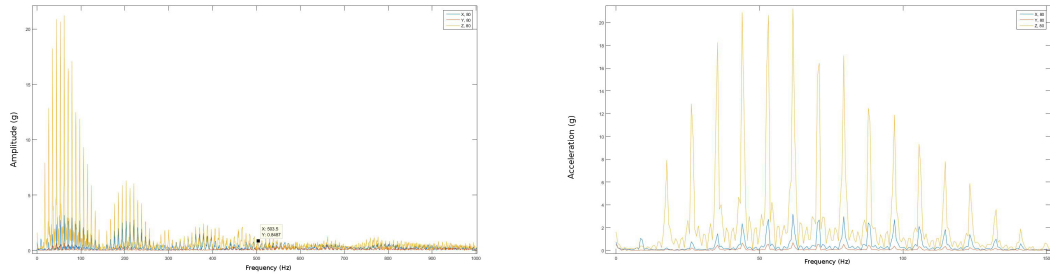


Figure 8: Most of the energy is found in 10-100 Hz range.

$$a_{centripetal} = \omega^2 r, \quad (7)$$

where  $\omega$  is the rotation speed of tyre and  $r$  is the radius of rotation.

## 2 Design

### 2.1 System-level design

The complete system will consist of energy harvesting source, energy storage for times when harvested energy is not available, AC/DC and DC/DC converters for maintaining required voltage levels in different blocks of system, accelerometer for measuring the acceleration in tyre and radio/microcontroller module for transmitting data from accelerometer. Figure 9 shows the power and data flow between subsections of system.

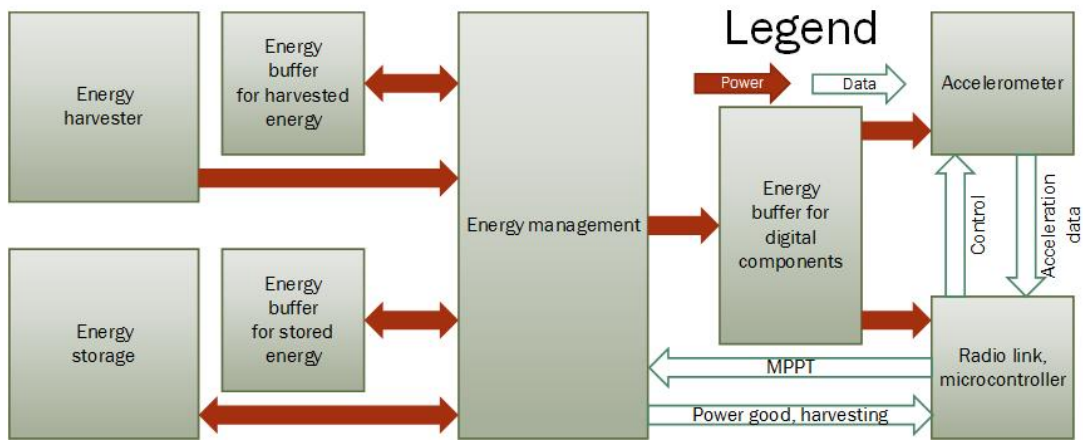


Figure 9: Block diagram of complete system.

Energy harvester can be any suitable source for electrical energy. Energy management section rectifies AC voltage and buffers the rectified voltage on a capacitor. The energy storage can be a supercapacitor or rechargeable battery. Both of these storage technologies can benefit from having a low equivalent series resistance (ESR) capacitor in parallel to supply any sudden peak currents. Energy management circuitry chooses whether to use harvested energy or stored energy and regulates the energy to voltage level compatible with the system. Digital components require their own local power buffer capacitors to supply high-frequency currents required by megahertz clocks onboard these circuits.

Microcontroller is used to manage the application layer of system. For example the microcontroller can send status updates over radio link more often if there is harvested energy available and reduce system power consumption when system is running on stored energy.

Next section presents details of expected power consumption and duty cycles for various components. A few components are selected to provide examples of suitable system power.

## 2.2 Power requirements of a system

The sensor system will be in three distinct states. One is sleeping, conserving power as much as possible while car is not moving. Second state is measuring, when the radio connection is off but electronics are active and gathering data. Third state is transmitting, when the data is relayed to drive computer in car.

Energy and power consumption are estimated by reviewing a few suitable components and their power requirements. Energy management is handled by a specialised integrated circuit (IC), for example LTC3331 [25].

Communication is handled by a Bluetooth-low energy (BLE) module, which contains a general-purpose microcontroller for application flow control. We use BLE113 [26] as an example of such module.

Finally there is an accelerometer which is used for gathering data out of the system, ADXL375 [27] is used as an example. ADXL is a low-power digital accelerometer with dynamic range of 200g. Table 1 summarises the estimated power requirement of each subsection of system. System level voltage is selected to be 2.5 V, as that is lowest voltage which LTC3331 can supply and allows all devices to function. Lowest possible voltage is selected to reduce the power draw.

Table 1: Current and power consumption of system at different activity levels.

Device	Sleep	Monitoring	Communicating
LTC3331	0.2 $\mu A$	80 $\mu A$	6 675 $\mu A$
BLE113	0.9 $\mu A$	275 $\mu A$	26 000 $\mu A$
ADXL375	0.1 $\mu A$	140 $\mu A$	140 $\mu A$
<b>Total power</b>	<b>3 <math>\mu W</math></b>	<b>1 200 <math>\mu W</math></b>	<b>82 000 <math>\mu W</math></b>

Current consumption levels for BLE113 and ADXL375 are taken from the datasheets of the components. Battery manager power draw is estimated by calculating required power to supply the rest of the circuit at 80 % efficiency. Power consumption is calculated from current draw with assumption that system voltage will be constant 2.5V.

Power consumption grows by orders of magnitude when the activity is stepped up to the next level. Therefore it is important to keep the system in sleep whenever possible, for example when the car is parked and wake up only periodically to check if movement has started. Monitoring starts once car is moving, and device will send brief pulses over the radio link when necessary.

When the power consumption is compared to values achieved in previous studies of energy harvesting, it can be seen that sleep current can be compensated by a reasonable harvester design. Powering constant monitoring would be a greater challenge, but with realm of feasibility. Providing power for continuous radio transmissions is not feasible even with current state-of-the-art harvester designs.

Next sections detail designs and preliminary analysis of electromagnetic generator designs. The initial designs are then evaluated based on their ability to supply

required power levels to circuitry.

## 2.3 Electromagnetic harvester design

### 2.3.1 Basics of electromagnetical vibration harvester

Electromagnetic harvesters utilise vibration to move a magnet inside a coil. The movement of a magnet causes a changing magnetic field, which gets coupled to a coil. The coil opposes the change in magnetic field by inducing electrical current in the device. A device could be built with a spring-loaded magnet to balance out the static acceleration of a tyre, an added benefit to spring loaded mechanism would be the utilisation of resonant frequency of the spring-mass system: as the system gets a shock, some of the energy would be in correct frequency range to make the magnet oscillate inside coil allowing generation of energy until next shock. The coil will also function as a damper to system, so no extra damping is required. Modern neodymium magnets do not lose their magnetisation by vibration, so long magnet can be reliable for a long time period.

A theoretical design of linear generator (LG) was made. Most common generator designs use a rotating magnet inside coils to generate alternating current. As the mechanical apparatus for converting the linear accelerations inside the tyre to rotational movement would add to complexity and cost of the tyre, generator is designed to use the linear motion as the power source.

Basic principle of operation of LG is similar to traditional rotational generator. A moving magnet creates alternating magnetic field which is coupled to coiled conductors. The conductors oppose this change of magnetic field by inducing an electrical current across their ends. The design can have multiple phases and poles, where phases refer to parallel connected coils and poles refer to serially connected coils. Multiple phase designs can have lower resistive losses in wiring, as the resistive losses are proportional to square of the current. However paralleling phases requires separate rectification for each phase, which leads to increased rectification losses. Adding poles to design increases the output voltage and frequency, but having a small airgap between the coils and magnets becomes critical to maintain efficiency of the generator [28].

Energy harvester designs sometimes use several poles to increase the frequency of the power output. This increased frequency allows to use smaller energy storage components such as capacitors to keep the device powered until next cycle. The characteristics of the tyre make this point irrelevant, as energy is available once per revolution of the tire when generator contacts the ground and when the contact ends. Any energy storage device has to maintain power until the next cycle, and no increase of the frequency while generator is in contact can alleviate that. Therefore number of poles is minimised to reduce complexity. Pole number is selected as two, so there is one negative and one positive pole. Mechanical design can utilise resonant vibration to function as energy storage device instead of electrical or electronic storage.

First design decision was whether to use a moving magnet or moving coil type of a design. Moving coil designs tend to have lighter moving parts which is a very

important feature in high-power designs where mass of the generator is large. On the other hand, moving coils require flying leads [29], which is a long-term reliability concern [5]. Boldea and Nasar [30, p. 203] conclude that moving coil designs aren't practically interesting, so the design is focused on moving magnet generator.

A rough model for designing initial prototypes was done previously by Elmes [31]. As the work verified the model experimentally and found the model to be reasonably accurate, it was adapted to form basis of linear generator model. The model can account for most of the key design parameters.

There are two different approaches to generator structure. One is magnets inside, and coils on the outer rim of the generator. Other is to use ring magnets on the outer rim and have the coils on the inside. Both methods have their advantages: Having magnets on the outside allows larger and therefore stronger magnets and creates horizontal support for the magnets as they move along the shaft. Having coils on the outside increases wiring radius which results in greater power if other parameters are held equal. In-depth study of both concepts is done to select optimal structure for generator.

The height of the generator is constrained at 45 mm to avoid contact between tyre rim and generator. Initially the height of the generator was selected to be 35-40 mm to leave some margin while still being as tall as possible. Lower weight is desirable to avoid unbalancing the tyre, but there is no specific absolute maximum mass for the device.

A method to counter the centripetal acceleration is needed to keep the magnet on the centre of the generator. Ideally, such method would always balance the magnet in the middle of generator against any external constant force, but active control is not achievable without adding to complexity and power consumption of the generator itself. Passive negative feedback method has to be used instead.

Springs are often chosen to balance the magnets, but as the centripetal acceleration grows exponentially with the speed of the car, any linear spring would be usable only for very limited range of speeds. Non-linear conical springs which have the added benefit of compressing into very small height are available.

Another approach would be to use two additional magnets fixed to top and bottom of the generator in repulsive configuration. Force between magnets is inversely proportional to fourth power of the distance [32], which leads to a strong negative feedback on the position of the magnet. Tornincasa et al. [33] proposed one such design, shown in figure 10.

Magnetic floating is an attractive solution, as magnets can be thin and they do not wear out with ageing. On the other hand, any imbalance in the magnets result in torque which causes increased friction. 11 This issue is further aggravated in designs where shape of the generator shaft is not a smooth cylinder. Therefore the design should have reasonably smooth and low-friction material on the inner shaft to minimise losses.

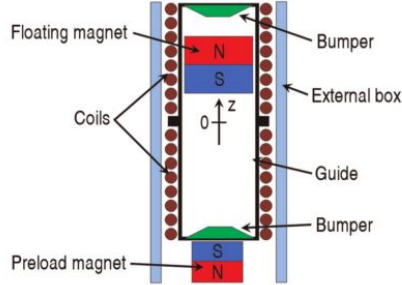


Figure 10: A magnetically balanced linear generator by Tornincasa et al. [33]

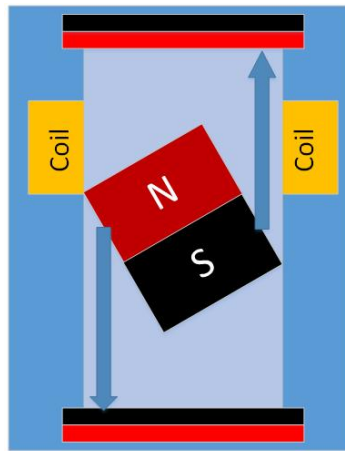


Figure 11: Angle in magnet causes torque which results in increased friction

### 2.3.2 Analytical model of electromagnetical vibration harvester

A common starting point for analysis of linear generator is to model the mechanical domain as Mass-Spring-Dampener system depicted in figure 12. A mass "floats" in system, a spring balances the mass towards centre and a damper represents frictional forces opposing any movement of mass.

Input  $Y$  is the force applied to the base of system, output  $U$  is the position of mass block relative to "zero". Zero is usually set to point where mass settles when no input, including gravity, is applied to system. Parameters  $m$ ,  $D$ , and  $k$  are mass, damping constant and spring constant of system, respectively. Input-output-equation in time domain can be written as:

$$m * \ddot{U}(t) + D * \dot{U}(t) + k * U(t) = Y(t). \quad (8)$$

As the force  $Y(t)$  is defined as  $Y(t) = m * a(t)$ , and the acceleration  $a(t)$  can be considered constant regardless of any reasonable mass  $m$  of system, equation (8) can be written as:

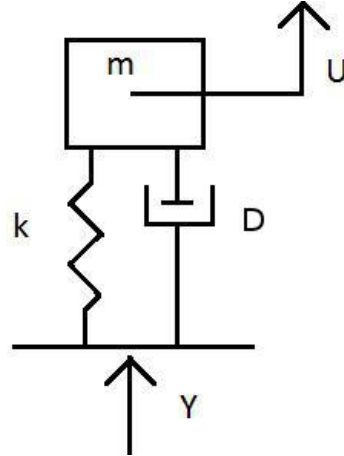


Figure 12: Mass-spring-damper system.

$$\ddot{U}(t) + \frac{D * \dot{U}(t)}{m} + \frac{k * U(t)}{m} = a(t). \quad (9)$$

This form is convenient for analysis, as the acceleration measurements from previous research are available and they represent real-world values. Mass \$m\$ can be considered constant, as the system does not exchange matter with surrounding environment. As magnetic suspension was selected, the parameter \$k\$ cannot be considered as a constant, but rather a function of mass position \$k(U)\$. Centripetal force can be considered as a constant DC-component of function \$Y(t)\$, and is not included in analysis of function \$k(U)\$. According to D. Amrani [32] force between two magnets can be approximated as

$$F(x) = \frac{3\mu_0 m_1 m_2}{2\pi} * \frac{1}{x^4}, \quad (10)$$

where \$F(x)\$ is force as a function of distance \$x\$ between magnets, \$\mu\_0\$ is the permeability of vacuum, \$m\_1\$ and \$m\_2\$ are magnetic dipole moments of magnets under examination. This equation is only valid when \$x \gg h\$, where \$h\$ is thickness of the magnet. As two magnets are used to suspend the rotor magnet, total force acting on mass becomes

$$F(x) = \frac{3\mu_0 m_r m_l}{2\pi} * \frac{1}{(x_0 + x)^4} - \frac{3\mu_0 m_r m_u}{2\pi} * \frac{1}{(x_0 - x)^4}, \quad (11)$$

where \$m\_l, m\_u, m\_r\$ are magnetic dipole moments of lower suspending magnet, upper suspending magnet, and rotor magnet. \$x\_0\$ is the distance to middle point of generator and \$x\$ is the displacement of rotor magnet from aforementioned middle point, positive direction being upwards. Figure 13 shows the system.

Regrettably, the expression (11) is very inaccurate for magnets where diameter is large compared to thickness of magnet, and the problems are compounded when distance between magnets is small. Therefore final design should be optimised using measurement data or finite element analysis (FEA) for determining \$k(U)\$.

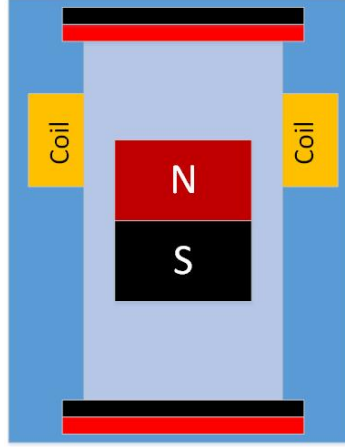


Figure 13: Linear generator with rotor magnet balanced by endstop magnets

Damping parameter  $D$  is likewise a function electromagnetic force acting on magnet, friction between magnet and stator and pneumatic damping caused by compression of air in generator. Tornincasa et al. [33] divided this damping parameter into three distinct terms to account for these different physical phenomena in damping. Let us call them  $D_{emf}$ ,  $D_{friction}$ , and  $D_{air}$ , respectively.  $D_{emf}$  represents power extracted from the system into electrical current, it can be written as:

$$D_{emf} = BIlsin(\phi), \quad (12)$$

where  $B$  is magnetic field affecting coil (presumed constant),  $I$  is current through wire depending on load and generator properties,  $l$  is total length of wire in coil and  $\phi$  is angle between coil and magnetic field, presumed to be  $90^\circ$ . Assuming the load impedance is the complex conjugate of coil impedance for maximum power harvesting, we can substitute the  $I$  with equations (2) and (4), which results in:

$$D_{emf} = B \frac{\varepsilon}{2 * Re(Z_{generator})} lsin(90^\circ), \quad (13)$$

where  $Z_{generator}$  is the impedance of generator. As the load impedance is complex conjugate of generator impedance, their series connection has only real (purely resistive) component. This assumption fails on real-world application with non-linear rectification and DC/DC conversion, but it can be used as a basis for analytical examination of the generator. As  $\varepsilon$  can be substituted with (2), we obtain:

$$D_{emf} = B \frac{-N \frac{d\Phi_B}{dt}}{2 * Re(Z_{generator})} lsin(90^\circ), \quad (14)$$

The relationship between  $N\Phi_B$  and  $Re(Z_{generator})$  can be further studied by writing

$$\Phi_B = \iint_{\Sigma(t)} B(r, t) dA, \quad (15)$$

where  $\iint_{\Sigma(t)}$  signifies possibility of loop area changing over time and  $dA$  is element of surface area. If we assume the coil to be a perfect tightly wound circle which does not deform over time, we can write the relationship between number of turns in coil, area of coil, and resistance of coil as:

$$R = N2\pi A \rho_{wire}, \quad (16)$$

where  $\rho_{wire}$  is resistivity of coil wire. Substituting (16) and (15) into (14) we finally obtain reasonably accurate expression for  $D_{emf}$  which accounts for all the design parameters affecting it:

$$D_{emf} = B \frac{-N \frac{d[\iint B(r,t) dA]}{dt}}{2 * N2\pi A \rho_{wire}} l \sin(90^\circ). \quad (17)$$

A few observations can be made from this equation: first, the magnetic field strength  $B$  and its derivative in respect to time increase the  $D_{emf}$  which signifies the electrically extracted useful power. Therefore it makes sense to use as strong magnets as possible, as long as other parameters aren't adversely affected. Second, both the number of turns and the loop area are as multipliers and divisors, which means they should be optimised to find best applicable values. Third, resistivity of wire limits power that can be extracted, so intuition would lead to minimising wire resistance. In practice the wire resistivity can be decreased by increasing wire diameter, which in turn leads to lesser number of turns in same volume and mass of coil. Therefore, also wire diameter and material should be optimised to find desirable compromise in generator design.

Next we examine  $D_{friction}$  in detail. Friction is modelled as Coulomb friction:

$$F_s = \mu_s N, F_k = \mu_k N, \quad (18)$$

where  $F_s$  and  $F_k$  are static and kinetic friction forces opposing movement,  $\mu_s$  and  $\mu_k$  are friction coefficients in static and kinetic situations and  $N$  is normal force along X- or Y- axis. Normal forces are estimated by using existing acceleration data and calculated mass of magnet. Coefficients of friction are looked up from supplier of stator material. Transfer between static and kinetic models is assumed to be a step, if velocity of magnet is 0 along Z-axis,  $\mu_s$  is used,  $\mu_k$  otherwise.

Finally, there is pneumatic damping of the system,  $D_{air}$ . In a closed tube, the central magnet can be thought as a piston dividing generator into two chambers. If there is insignificant airflow between chambers, any force caused by pressure deltas between chambers act as a spring. However, some airflow is to be expected due to clearance between magnet and stator. Tornincasa et al. [33] modelled this effect by adding a virtual centrepoint for pneumatic spring, this centre moves through a virtual damper which models the airflow between chambers. End result is that pneumatic spring takes some energy from movement, and this energy stored into pneumatic spring is dissipated as the centre moves until potential energy stored in the spring is zero.

The force from pressure differential is:

$$F_{\delta p} = \frac{\pi d^2}{4} (p_{lower} - p_{upper}), \quad (19)$$

where  $d$  is diameter of magnet and  $p_{lower} - p_{upper}$  are pressures in chambers. Pressures can be estimated from ideal gas law:

$$pV = NRT \quad (20)$$

where  $p$  is pressure,  $V$  is volume,  $N$  is amount,  $R$  is ideal gas constant and  $T$  is temperature. Temperature is assumed to be constant. Initial pressure is assumed to be same as tyre pressure and magnet is assumed to be exactly in midpoint at start. Change of volume can be calculated from change of height caused by movement of the magnet.

Mass flow between sections can be estimated with equation given by Fox et al. [34]:

$$\dot{m}_{1 \rightarrow 2} = \frac{\rho \pi d \delta_r^3}{12 \mu h} (p_1 - p_2), \quad (21)$$

where  $\rho$  is air density,  $\delta_r$  is radial clearance,  $\mu$  is dynamic viscosity and  $h$  is the height of magnet. [33]

There is also frictional dissipative force as the air passes along the edges of the cylinder. This frictional force has magnitude of:

$$F = \mu * \rho * \frac{\pi d h \dot{z}}{\delta} [35]. \quad (22)$$

Analytical expressions for the equations governing the mechanical movement of magnet inside generator have now been identified. Some of the non-linear functions are hard to solve analytically, therefore experimental or FEA methods should be used for creating approximations for these functions.

The analytical effect of these parameters is summarised in table 2

Table 2: Effect of parameters of generator

Parameter	Increasing	Decreasing
$N_{turns}$	Higher voltage	Smaller size, less wiring resistance
$N_{pole}$	Increased frequency	Decreased frequency
$l_{pole}$	More space for wiring	Higher voltage, smaller size
$A_{loop}$	More power	Smaller length of wiring
B	Increased power	Smaller magnets
$r_{wire}$	Decreased wiring resistance	More turns in same space
$\delta_r$	Stronger side walls	Increased efficiency

### 2.3.3 Experimental and FEA modeling of electromagnetic harvester

As some parameters of the harvester are difficult to solve analytically, these parameters are solved using experimental and FEA methods. First one of these difficult interactions is the magnetic force between rotor magnet and balancing magnets. A magnetics FEA software FEMM [36] was used to create an axisymmetric model of magnets in generator. Figure 14 shows the used model. Model has two biasing magnets made of N40-neodymium alloy configured to repel an identical rotor magnet. Magnets have height of 2.5 mm and diameter of 11 mm, walls of generator are modelled as air. Generator has total height of 25 mm, leaving rotor magnet 17.5 mm room for movement inside generator.

Weighted stress tensor integration over rotor magnet volume as implemented by FEMM was used to determine FEA value for net magnetic force acting on rotor magnet. A LUA script was used to move the rotor magnet from bottom of the generator to top in 0.1 mm increments and values obtained from analysis were exported as CSV data for plotting in a spreadsheet software as well as to create a lookup-table for MATLAB/SIMULINK simulation. Figure 14 shows the force on magnet, positive force meaning force towards the upper magnet and zero height being at the bottom of cylinder. For reference the centrifugal force acting on magnet was also calculated at various speeds, assuming weight of the magnet is 1,67 g and radius to bottom of generator is 275 mm.

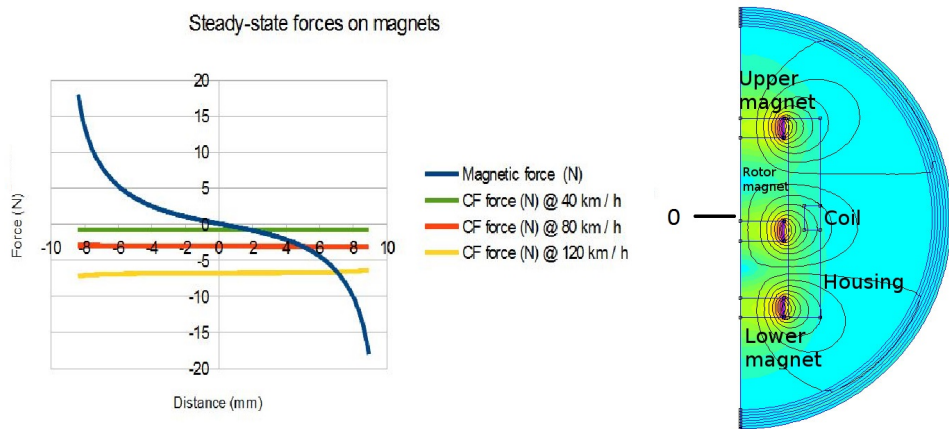


Figure 14: Steady-state forces acting on magnet

It can be seen that net force on rotor magnet is dominated by the magnetic forces at lower speeds. Centrifugal force on magnet becomes significant at higher speeds, but even at 120 km/h speed the rotor magnet will stay clear of the bottom. Second use for this FEA analysis is to create look-up table for flux linkage into coils of generator. The methodology was similar to determining forces affecting the rotor magnet: a LUA script was ran to sweep possible magnet positions, and look-up table of flux linkage into coils was created. For the purposes of analysis, difference of flux linkage was calculated between each point. The change of flux linkage is a very

important parameter, as the power generated is proportional to  $\frac{d\Phi_B}{dt}$ .

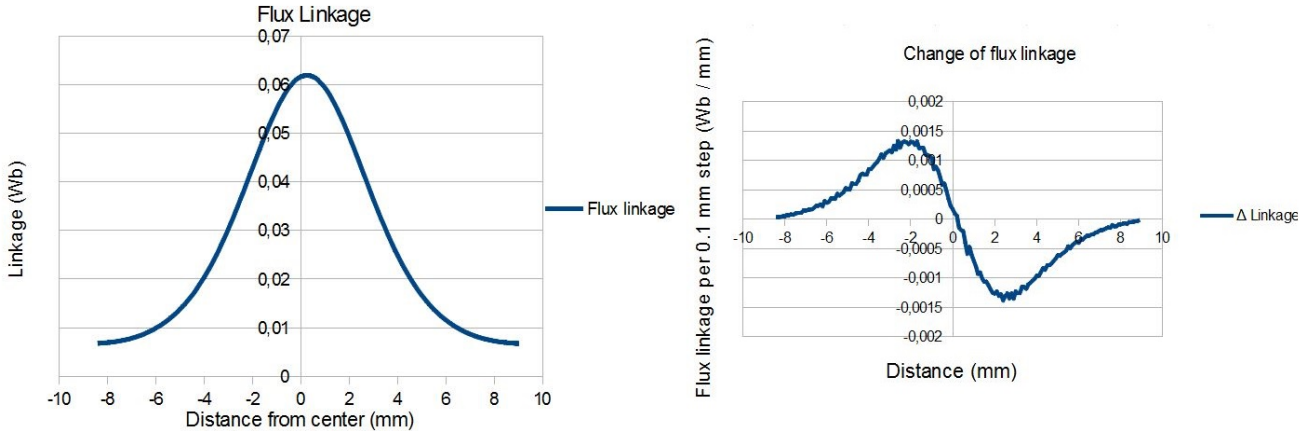


Figure 15: Flux linkage and rate of change in 0.1 mm steps in generator.

Based on these results, a magnet moving at the speed of  $0.1\text{mm/s}$  would induce voltage of up to  $1.5\text{mV}$  in each winding of the coil. If we assume coil to have 100 turns, travel length of the magnet to be 1 mm, and frequency of magnet moving inside generator to be 10 Hz the peak voltage out of generator would be sufficient to power the circuitry and charge battery of sensor.

A prototype generator was built to test the concept feasibility and identify any practical issues in the generator construction. Generator was machined out of 21mm diameter nylon tubing with 12 mm inner diameter. A groove was machined on the outer diameter to hold the coiling in place. Inner diameter of the groove was 14 mm and height 3 mm. 0.1 mm diameter wire was used to build the coil. To determine the number of turns in coil, coil resistance was measured to determine the length of wire and number of turn was calculated using known length of loop turn and total length of wire. Coil resistance was 42 ohms as the resistance of wire is approximately 2.2 ohms / meter the total length is approximately 19 meters. As one loop has length of 44 mm, coil had roughly 400 turns.

The prototype was connected on a Brüel & Kjær shaker type 4905 and driven using Brüel & Kjær power amplifier type 2707. Input signal was generated using NI-USB6218 DAQ and output was measured directly from leads of the generator. Vertical displacement of generator was limited to 7.5mm. Output signal was a sine wave with amplitude of  $\pm 5$  volts, which was amplified by gain of 8 above frequencies of 30 Hz. At lower frequencies the gain was limited to stay within allowed displacement. Measured graphs are shown in figure 16.

At low frequencies the magnets do not overcome friction and only measurement noise is present in signal. In addition to white noise in measurement there is a sine wave with amplitude of few millivolts which correlates with the excitation signal. The measurement noise is insignificant when compared to signal generated my moving magnet.

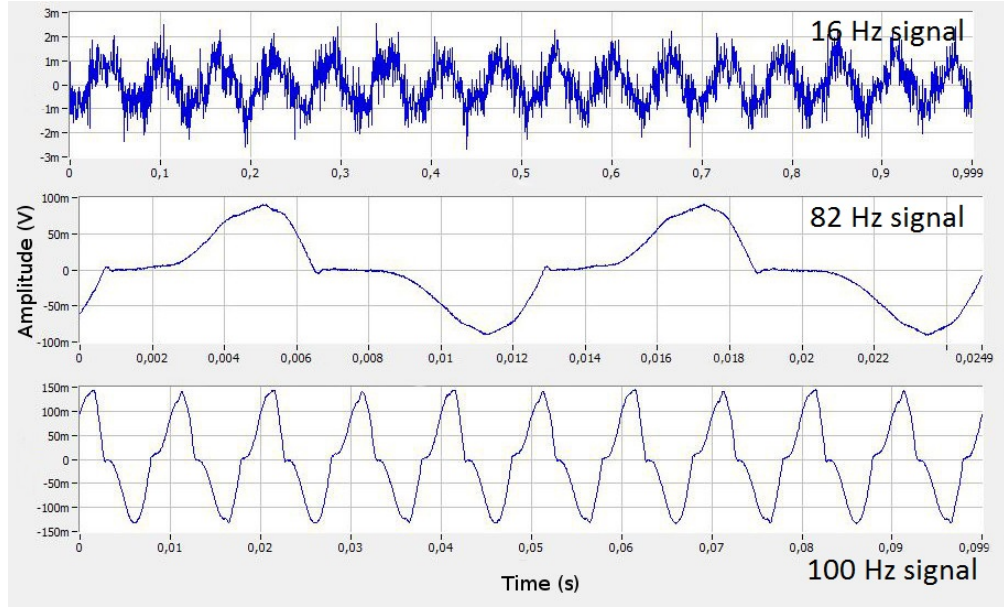


Figure 16: Measured open-loop voltage outputs at various frequencies

At low frequencies the magnet cannot overcome the friction and only noise is present in measurement. Around 82 Hz the magnet could move inside shaft, producing peaks with roughly 100 mV peaks. The magnet stops in between of the peaks which is seen as valleys of no voltage being produced.

Peak voltages of roughly 150 mV were achieved at 100 Hz. The magnet is in almost constant motion, a brief stop can be seen when the magnet changes direction.

While 150 mV is notably less than the few volts predicted by Simulink model, the basic operation principles was validated by quick experiment. The difference in output voltage is probably due to imprecise construction in prototype harvester. As the concept was proven, the design of generator was finalised. Next section details the exact construction of final electromagnetic generator.

#### 2.3.4 Mechanical design of electromagnetic harvester

Few practical issues became evident during construction of prototype generator. Machining grooves to plastic tubes caused warping to tube, which prevented magnet from moving inside coils. Shallow grooves would not keep the coils in place, as wires being loose would fall off the groove. The tube did not offer any reasonable mount point for a printed circuit board.

Issues with grooves were solved by selecting a tube with minimal wall thickness and using separators to contain the coil. A separate housing was designed to hold the tube and to offer mounting points for the circuit board.

A layered design was made for the harvester. On the bottom is a solid square with 35 \* 35 mm sides and holes for screws on corners. Next layer has a hole for the bottom magnet, third layer has hole for the tube. Tube has a spacer in middle to

hold the coil below midpoint. Top half of harvester is symmetrical to bottom.

## 2.4 Piezoelectric harvester design

### 2.4.1 Basics of piezoelectric energy harvesting

This section details experimental identification of properties of piezoelectric element to be used in harvester. A testbed with impactor providing excitation is used to generate experimental values for power output and voltage at various operating conditions for the piezo element.

Thunder(TM) piezos have been used in previous studies of piezoelectric harvesting and they have produced promising results [16], so they were selected as the piezoelectric element for this thesis.

Series of tests were ran to determine characteristics of piezoelectric power generation under impacts. Mossi et al [37] have produced a recommended test process for Thunder piezoelectric actuators shown in figure 17.

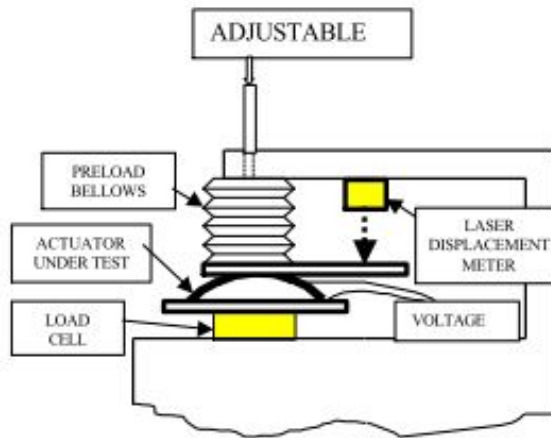


Figure 17: Recommended evaluation platform for Thunder piezos [37].

This setup was replicated using a solenoid actuator as impact force generator, precision scale as load cell to measure impact force and oscilloscope to view output waveforms. An eraser was cut to shape to act as preload bellow to spread the impact over larger surface area of piezo, displacement was not measured. The test setup is shown in figure 18. An electronics prototyping platform, "breadboard", was used to house test electronics including resistive ladder and Arduino to trigger the solenoid at adjustable duty cycles. Load force was controlled by setting the stroke length of solenoid shaft and fine tuned by adjusting voltage over solenoid.

The measurement results are shown in figure 19. Output voltage scales with square of impact force, which makes sense as work done can be expressed as  $W = F \cdot d$ , where  $W$  is work,  $F$  is force and  $d$  is distance force acts on object. As the displacement of piezo grows with the applied force, total work and therefore energy grows with both terms.

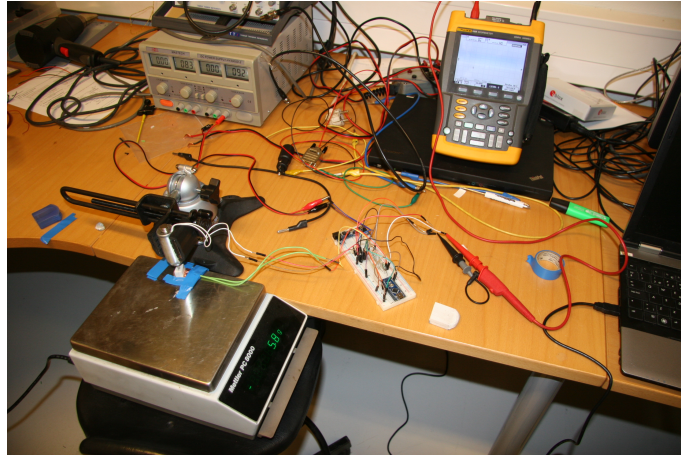


Figure 18: Test platform for piezo characteristics.

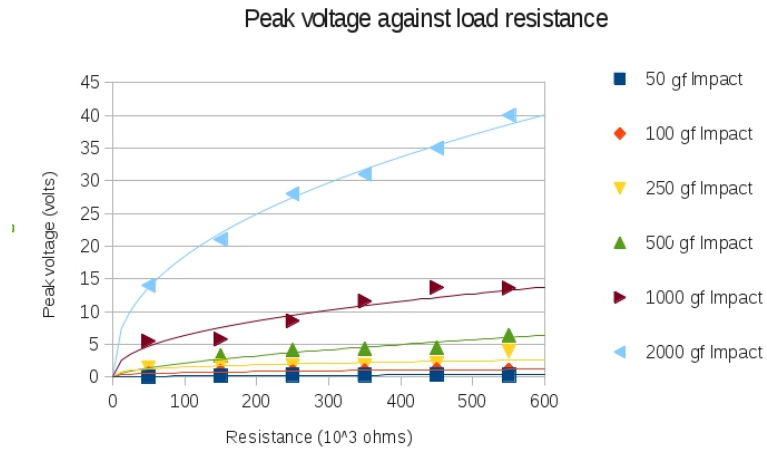


Figure 19: Measured output voltage at different loads and impact forces.

Peak voltage grows with the load resistance. This makes sense in both voltage source and current source models, as the capacitor starts to discharge through load resistance instantly when voltage is applied over it. The relationship between voltage and load resistance seems to be logarithmic, which would be in good agreement with the logarithmic discharge curve of capacitor-resistor system. Peak voltages were read out from digital display and they can be considered reasonably accurate.

The time constants for voltage halving was graphically measured from oscilloscope waveforms, and this data was used to calculate the capacitance of TH-5C. These measurements are a lot less accurate, as readouts from oscilloscope screen have resolution of approximately half of line division, leaving accuracy of measurements at  $\pm 2.5\text{ms}$ . These results are plotted in figure 20

The half-time data can be used to calculate capacitance of piezo using the RC-time constant of circuit:

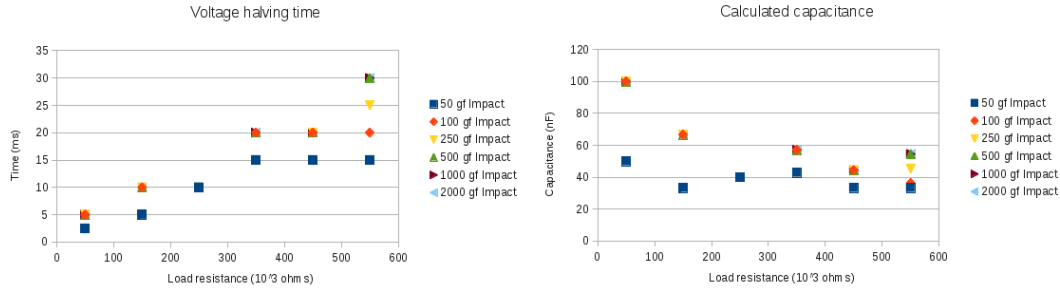


Figure 20: Measured half-time of system and calculated capacitance of piezo.

$$C = \frac{t}{-ln(\frac{1}{2})R} \quad (23)$$

TH-5C provides value of 39nF as the capacitance, while these calculated values are notably higher and rise with the loading of piezo. Most likely explanation of this observation is the mechanical response time of system: solenoid plunger will take some milliseconds to reach new force equilibrium, and this effect becomes more pronounced at smaller time constants of RC-system. Using the known voltage and capacitance energy and peak power in impact can be determined:

$$E = \frac{1}{2}V^2C \quad (24)$$

$$P_{peak} = \frac{V^2}{R} \quad (25)$$

The calculations are plotted in graph 21. As these calculations are based on inaccurately measured time, they should not be used as reference for any further calculations. However, trends can be seen in these values.

Interestingly the peak work done by piezo to resistor seems to be almost constant on all load levels. This is probably a consequence of logarithmic voltage-load relationship described above. There is a possibly significant result based on these findings: total energy obtainable from harvester grows with load resistance. However, this is applicable only for resistive load under impact-based energy generation.

Based on these results, an electrical equivalent model of circuit was designed. The model is shown in figure 22. Model has two parallel current sources, one to simulate impact of plunger on piezo and other to simulate release of the impact. Capacitance in parallel is set to 39 nF as given in datasheet, load resistance is parametrised to step through the experimental values.

Model was tuned by first calculating the total current transfer to reach the open circuit voltage over capacitor. Then maximum current of current sources was matched to reach peak voltage over highest load. The simulated data is plotted figure 23.

The experimental and simulated data are not in a good agreement. While maximum and minimum load voltage and power are close to estimated values, this is

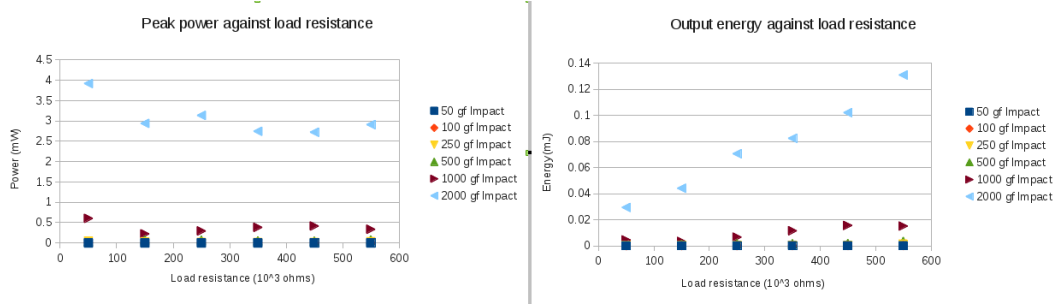


Figure 21: Calculated piezo power and energy output

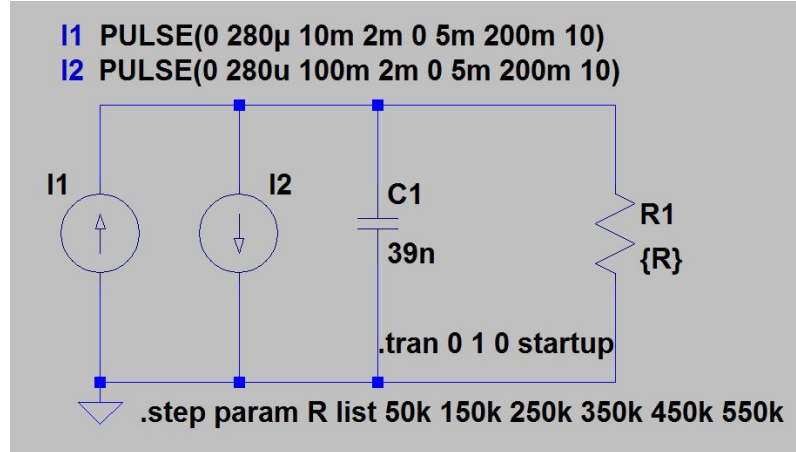


Figure 22: Equivalent model of piezo in LTSpice simulator

by design as model is tuned to these measurements. Problems occur in interpolating the results, as output voltages are notably higher than measured values. This provides a result which sets the maximum power load near the value which provides output voltage of half of the open loop voltage. This is especially interesting as LTC3331 datasheet [?] suggests to set the circuit to track the load at this same half-point of open loop voltage. Both LTC3331 and LTSpice are made by Linear Technology, so independent verification of this result would be needed.

## 2.5 Electronic design

### 2.5.1 Simulation of circuit

As the focus of work is in energy harvesting, only analog sections related to energy harvesting are simulated. Digital loads are simulated as current sinks. This section details the simulation model used to validate the design of circuitry.

The analog sections of circuit were simulated using LTSpice IV [38]. Microcontroller, radio link and accelerometer were simulated as resistive load. Battery was modelled as a voltage source with high-value capacitor and low-value resistor in series.

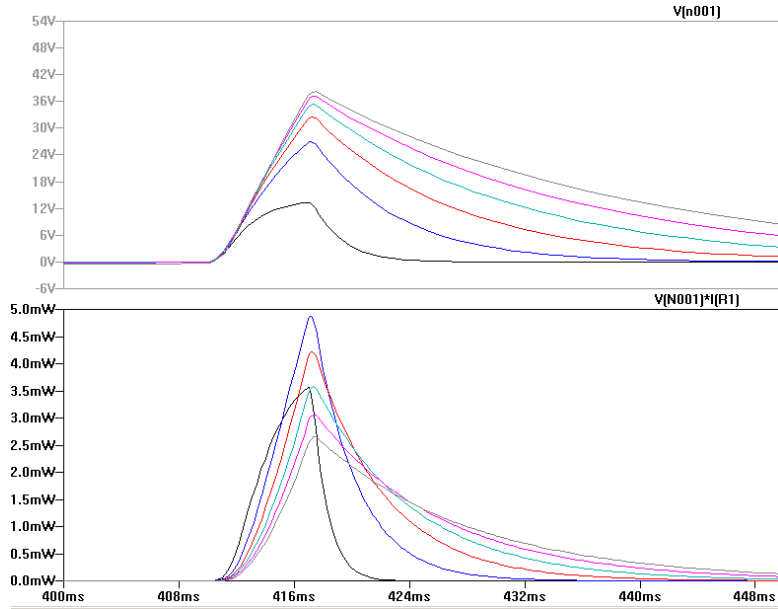


Figure 23: Simulated piezoelement output voltage and power waveforms. Loads are stepped through list to match experimental values at 2000 gf impact force. Black: 50k; Blue: 150k; Red: 250k; Turquoise: 350k; Violet: 450k; Gray: 550k

Piezoelectric harvesting was modelled both as high-voltage source with capacitor in series and current source with capacitor in parallel. Electromagnetic harvesting was modelled as low-impedance low-voltage source.

LTC3331 presents an interesting opportunity for maximum power point tracking (MPPT). While the impedance of individual components cannot be tuned in real-time, the microcontroller can determine rotation frequency of tyre from accelerometer readings and determine the maximum power point. LTC3331 can adjust the target voltage for energy storage buffer capacitor, which enables MPPT-control of system.

The simulation model is shown in figure 24. Connections were adjusted as needed to generate simulation data for different purposes, such measuring energy efficiency, transient response, MPPT etc.

The simulation model was used to validate basic operation of circuit. Circuit operates as datasheet specified. MPPT algorithms can be developed after the experimental results from energy harvesting are obtained.

As the basic operation of circuit has been validated, next step is to design the detailed schematic for the circuit. The next section details schematic design of the circuit, starting from top-level diagram and connections between blocks, followed by detailed design of each subblock.

### 2.5.2 Schematic design

The printed circuit board (PCB) schematic is a logical representation of the components and how they connect to each other. The schematic is designed in accordance

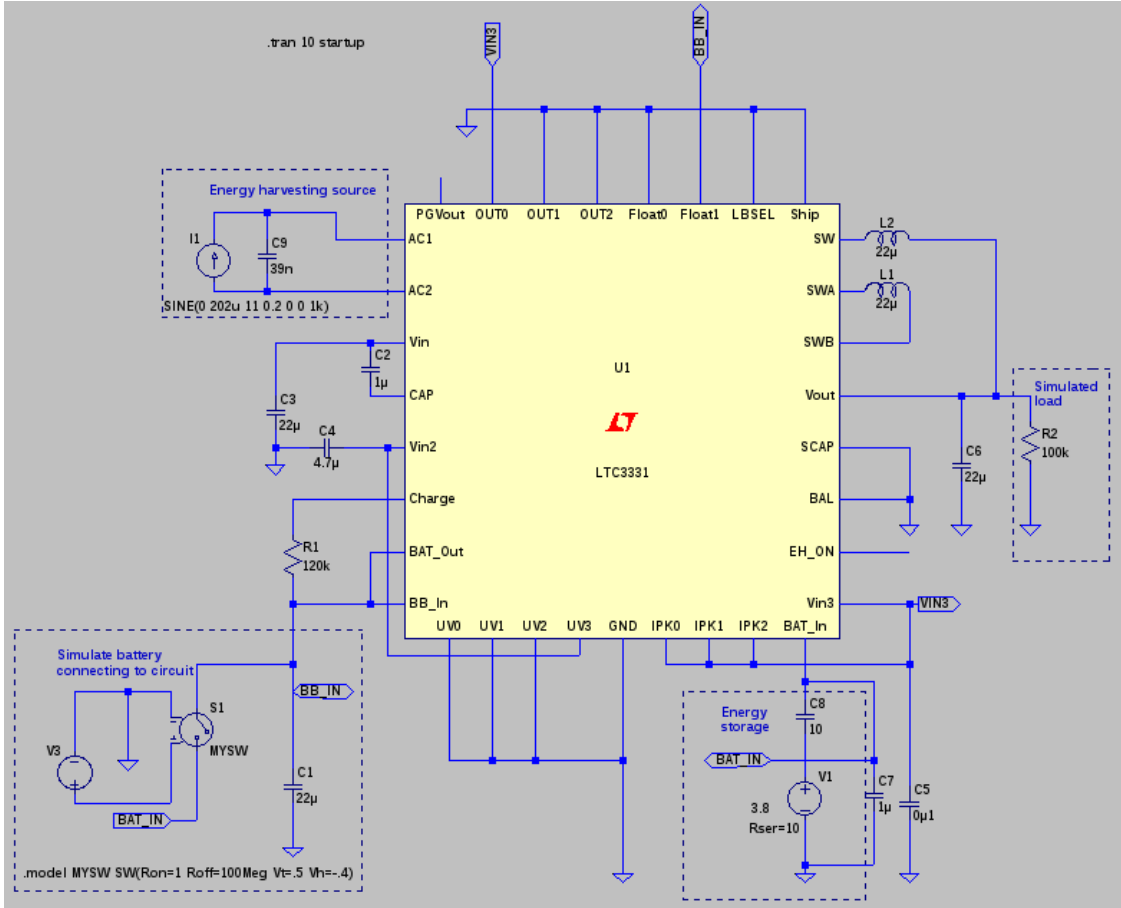


Figure 24: LTSpice [38] simulation of electrical circuit

to datasheets, reference designs and application notes of main circuit components. This section details the schematic diagram of the circuit.

As the design operates in high-vibration environment with wide temperature variations, special care is used to select components which have well-defined temperature and mechanical characteristics.

As the circuit is a low-power design, careful attention has to be paid to parasitic properties and non-ideal behaviour of components. For example electrolytic capacitor can have leakage current of several microamperes [39], which is in the same order of magnitude as the targeted sleep current consumption of system. Likewise any signalling current should be kept at minimum.

Another important point of view is the modularity and testability of the circuit. All critical lines have provision for testing and debugging for development and verification of circuit functionality. Figure 25 shows the interconnections in system, drawn in KiCAD [40]. The power supply can be cut off to separate sections of circuit for current measurement as needed. This has additional benefit of leaving places for power supply filtering components in case some section of circuit emits electrical noise through power supply lines.

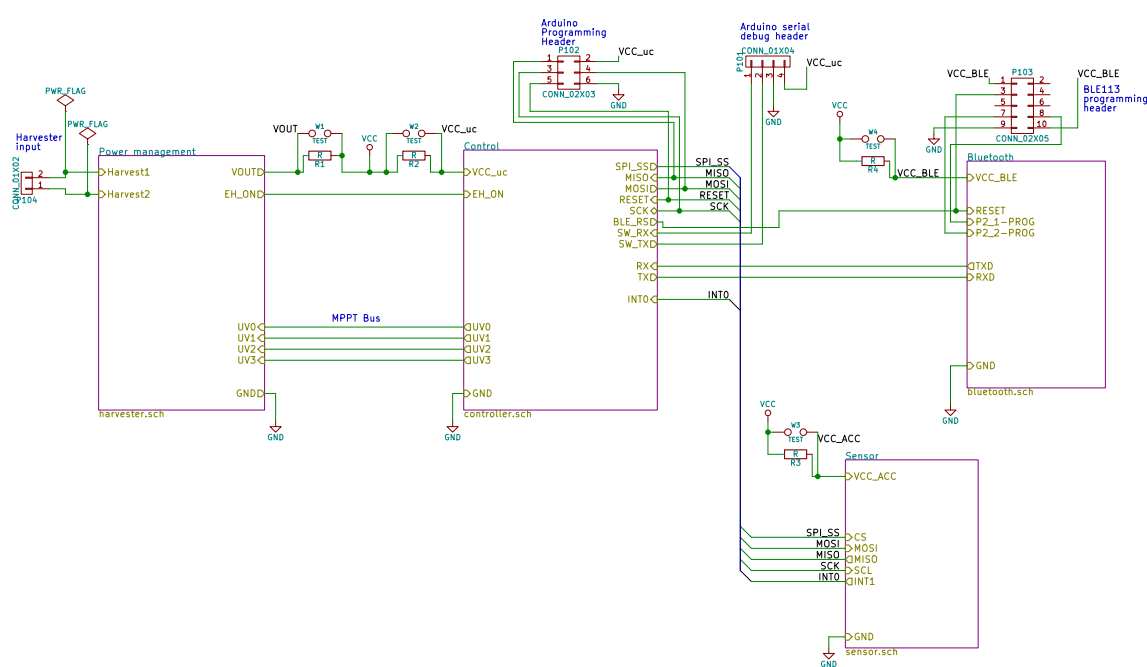


Figure 25: System level design of electronics

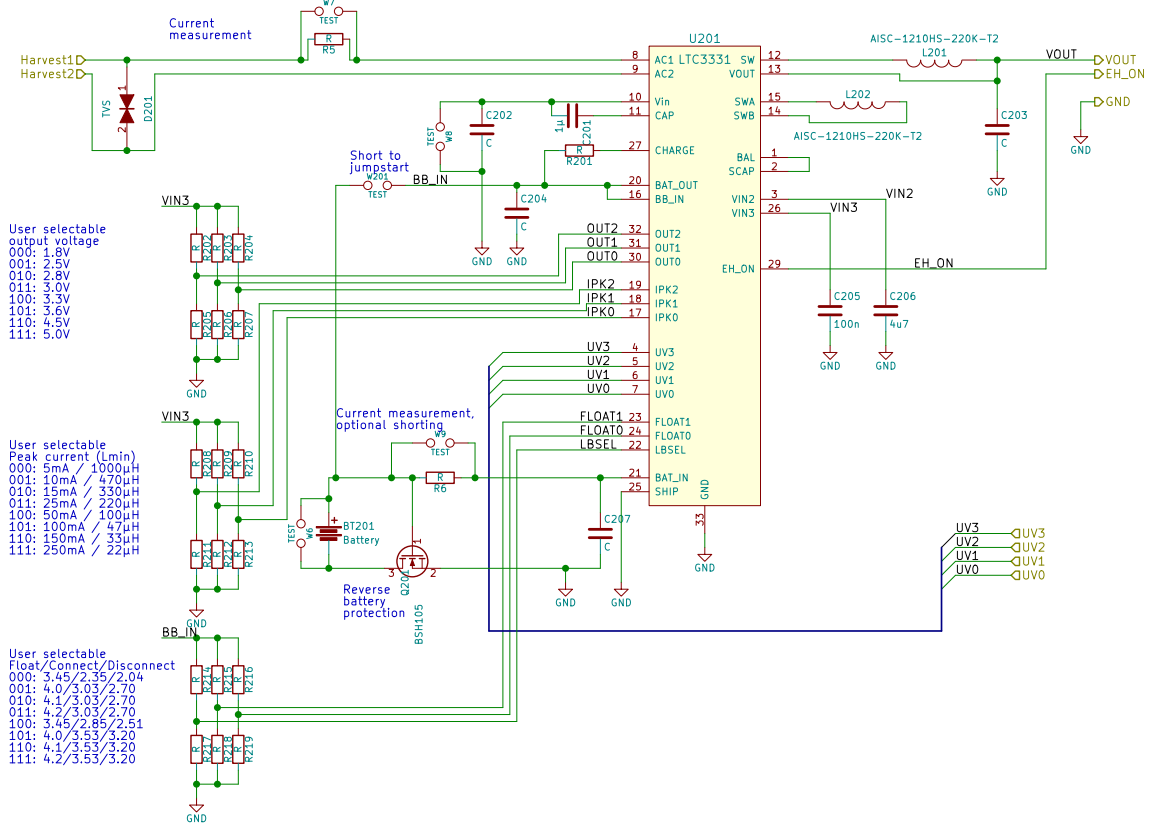


Figure 26: Power supply with harvesting input, battery management and SMPS voltage output.

Power supply has some conflicting requirements, as any noise in power degrades radio and measurement performance, but on the other hand the power supply should be efficient switch mode power supply to keep power consumption at minimum. LTC3331 has switch-mode power supplies which can be used to generate supply rails for the rest of circuit, these are used and noise is dealt with by passive filtering. Most of the power supply design 26 is relatively straightforward application of ideas presented in LTC3331 datasheet, but a few special considerations have been given to tailor the power supply for application. Device is configurable by soldering appropriate resistors, and the energy harvesting MPPT can be controlled by external microcontroller using signals UV[0:3].

Battery configuration allows different chemistries to be tested, as the under- and overvoltage lockout levels are user selectable. If a non-rechargeable battery is desired, battery charging can be disabled by omitting resistor R201.

Central controller is built around ATMEGA328 [41] microcontroller. The controller uses SPI and UART serial communication between sections of the system, and it has parallel connection to LTC3331 to set the energy harvester voltage levels for MPPT. LTC3331 has EH\_ON output, which rises to logic high level of approximately 4.8 volts when the circuit is being supplied by harvested energy rather than by a battery. This voltage level is above the circuit supply voltage, and therefore interfacing

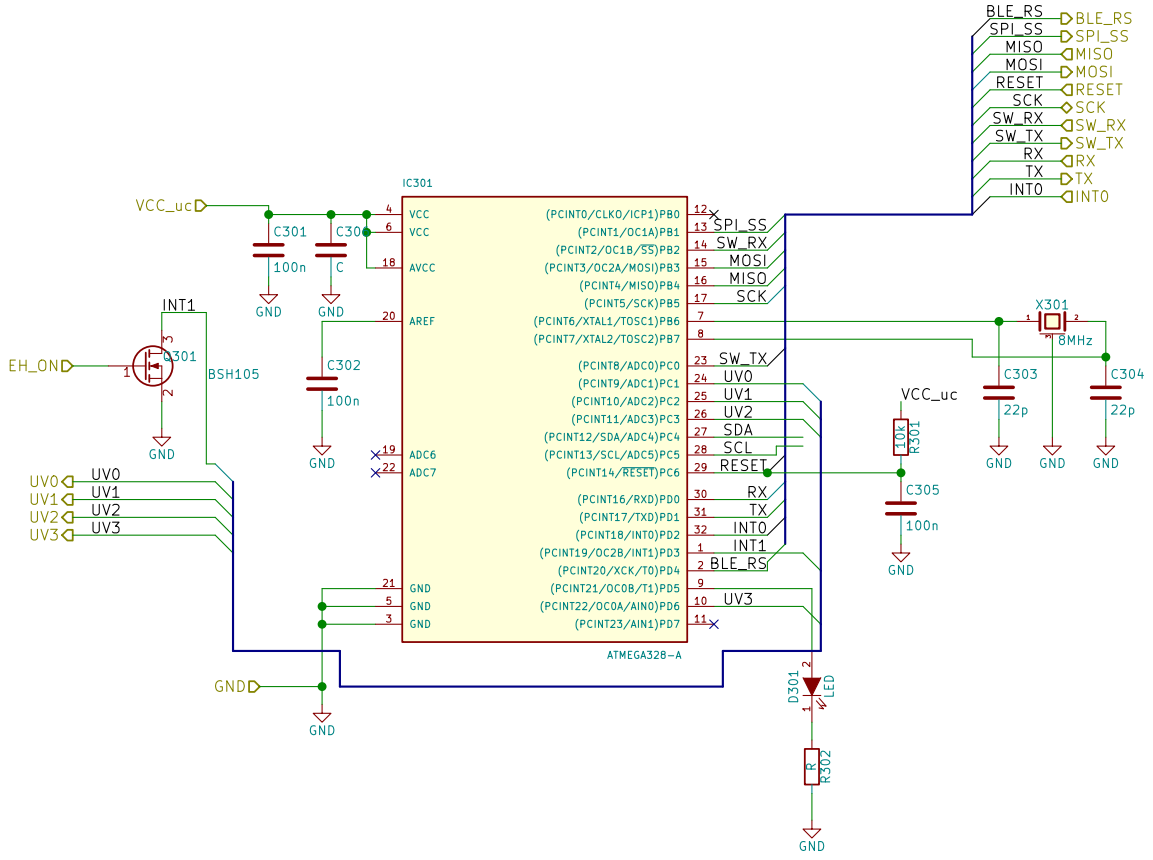


Figure 27: Control circuit with external interrupts from sensor and energy harvesting.

it directly to ATMEGA328 would be damaging. Interfacing is done by N-MOSFET BSH105 [42] and internal pullup-resistor on ATMEGA328. When harvested energy is available, pull-up of ATMEGA328 becomes grounded through BSH105. This causes somewhat significant current leakage, in range of tens of microamperes while pull-up is being pulled down. However this leakage is present only while harvested energy is available, so it will not drain the battery of circuit. While harvested energy is not available, the MOSFET is shut off. Special care was taken to select a model of MOSFET with small off leakage to avoid drain while system is being run on battery power, BSH105 is specified to have leakage in range of tens of nanoamperes.

Most important power saving is achieved through careful design of software. Sleep power states of ATMEGA328 consume minuscule amount of power when compared to active state, therefore minimising active time of circuit is a high priority. If the program is not CPU time limited, clock rate can be scaled down to 1 MHz using internal clock divider. Maximum CPU frequency can be increased by selecting another crystal, but increasing clock frequency will require higher supply voltage which in turn leads to higher overall power consumption in entire system.

Radio link is implemented with BLE113 module. The module could act as stand-alone controller for the system, but radio link has been separated from control logic to allow focused study of different sections of circuit. Schematic 28 is very simple, power supply is decoupled by bypassing capacitors as recommended by datasheet

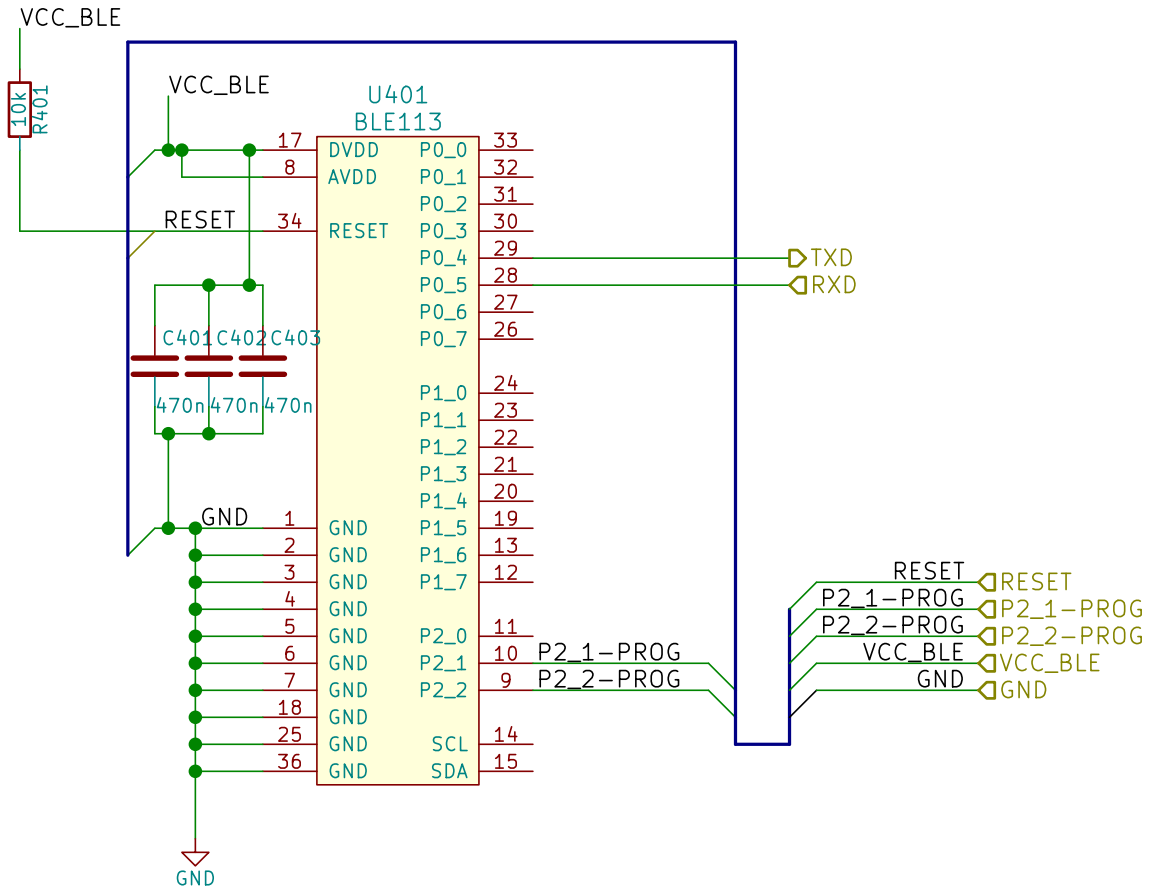


Figure 28: Bluetooth connectivity built with BLE113 module

and programming header has been brought out. Communication to microcontroller is handled by universal asynchronous receiver/transmitter (UART) communication using 2.5 V level signalling.

BLE113 can be forced to sleep by external control if needed and it can operate autonomously while main controller is sleeping. Data payload can be up to 20 bytes per packet as specified by BLE protocol [cite](#), maximum data throughput is defined by connection interval. As transmitting data consumes active time and therefore power, data transmissions should be minimised while harvested energy is not available.

There is an accelerometer ADXL375 onboard the PCB to study applications of tyre sensor system. Schematic of sensor section is shown in figure 29. The power supply section has a separate digital Input/Output (IO) supply voltage which is further filtered for analog sections of board by FB501 and C502. Both supplies are fed by same system level power bus from LTC3331.

ADXL375 is capable of both SPI and I<sub>2</sub>C communication, SPI communication was selected to facilitate faster communication to minimise time control circuit has to be in awake and to avoid additional power drain through the required pull-up resistors of I<sub>2</sub>C bus. On the other hand, the circuit has a design feature which requires usage of OR gate to avoid SPI sequence being interpreted as I<sub>2</sub>C command. The OR was selected to be SN74AUP1T32 [43], which has minimal static power

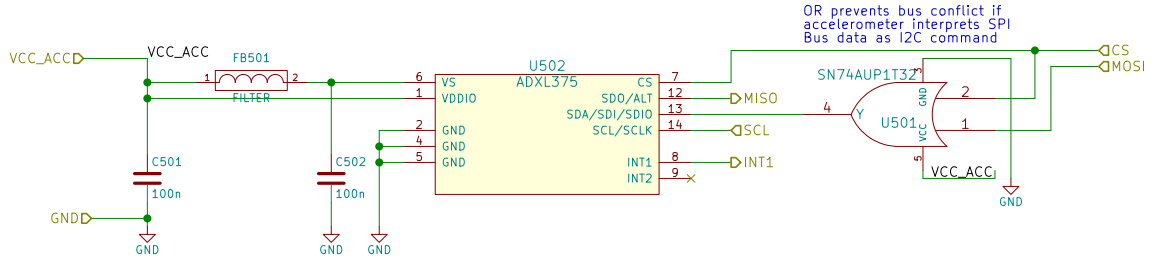


Figure 29: Accelerometer circuit

current consumption of 0.1 microamperes.

As the circuit will be subject to extreme accelerations, all the components should be surface mounted. This gives maximal solder pad area to height ratios, which helps to maintain the integrity of circuit. Larger components, such as inductors can be additionally glued for increased mechanical reliability.

The estimated current draw for each of the subcircuits dominated by the main integrated circuit of each subcircuit. The power consumption estimates were presented in section 2.2 table 1.

As the schematic was finished, next task was to design the layout of the circuit. Next section describes the design process of laying out the circuit and shows the completed design of circuit board.

### 2.5.3 Circuit layout

The PCB layout defines the physical placement of the components on the circuit board. Process of laying out the circuit as well as the structure of printed circuit board is described in this section.

Usually circuits are laid out by defining the outline of the board. Then any mechanical constraints, such as mounting holes and connectors are placed. Next step is to place the main ICs. As the main features of circuit are defined, subsections of circuit is planned. Critical and sensitive components such as crystals and antennas are placed as first priority. Then the power supply lines and power supply components are placed, in this case the inductors and capacitors of SMPS are placed as close as possible to relevant pins.

As the design operates in high-vibration environment with wide temperature variations, special care is used to select components which have well-defined temperature and mechanical characteristics.

The circuit is laid out on 4-layer PCB, where inner layers are dedicated to ground and power planes. This means that power supply decoupling needs a lot less care than on 2-layer board, generally a via straight from power pin to relevant plane gives low-impedance supply to circuit. Power supply decoupling capacitors are still placed as close as possible to relevant pins and power supply pins are fed directly from capacitors when possible to minimise power supply noise leaking into power planes.

Finally the rest of the circuit is laid out. As the currents flowing on board are relatively small and signal rates are low, routing can be rather carefree on non-critical

sections. Final board is shown in figure 30. Energy harvesting section is at left, radio is on top, control section is at right and accelerometer is at bottom.

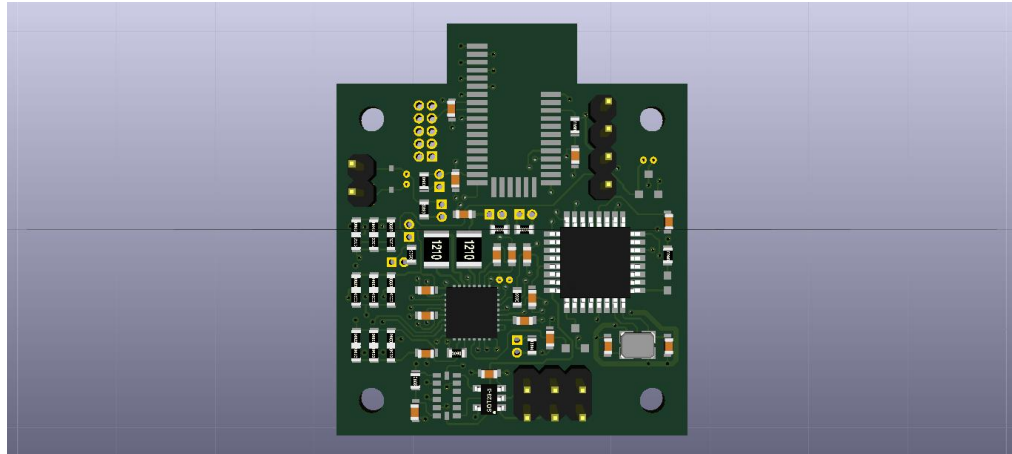


Figure 30: Render of the final PCB

The borders between sections are most clearly visible in the power planes of design shown in figure 31. Power planes for each subcircuit have been separated for testing the current consumption, and therefore the outlines of power planes follow the outlines of subcircuits.

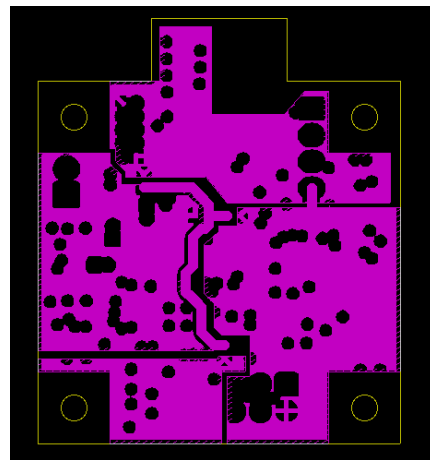


Figure 31: Power planes of the PCB

In addition to mechanical and electrical properties, the PCB also acts as heat sink for mid-power components. In this circuit only LTC3331 needs special attention to thermal design, it is cooled by several vias under the pad of circuit into ground plane. As copper is excellent conductor for heat, any thermal output from LTC3331 gets coupled to ground plane where it can spread to a wider area.

Battery holder is only large component in design where G-forces might cause a

problem. The holder is on the backside of the pcb, where it can be mounted using adhesives or it can be supported by harvester top.

## 2.6 Mechanical design of harvester

This section details the mechanical considerations for both harvester types. First material options are explored, then the design for generators is presented.

Material for the generator has a few requirements. It has to have at least as good temperature characteristics as the magnet being used and it must be hard enough to not deform under impacts. Low friction coefficient is desirable as this leads to smaller losses, and long time durability under wear is of course desired. Being lightweight and easily machinable are also desired characteristics. As the generator is small, volumetric cost of the material is of little concern. For the electro-magnetic generator design material ferromagnetism has to be considered. Table 3 has comparison of different materials considered for the application.

Table 3: Materials for the shaft of generator [44], [45], [46] [47].

Material	Hardness	Friction	Durability	Temperature
PTFE(Teflon)	Very low	Lowest	Lowest	-190... + 250 °C
Polycarbonate	Very high	High	-	-60... + 125 °C
PA 6 (Nylon)	Low	Medium	High	-40... + 80 °C
Oil-infused Nylon	Low	Very low	Very high	-20... + 105 °C
Acrylic	High	-	-	-40... + 70 °C
Polyacetal (POM C)	Medium	Low	Low	-50... + 105 °C
Carbon fiber	Highest	Highest	High	... + 80 °C

There is no single best material for the harvester. Polycarbonate and carbon fibre would have excellent mechanical strength but they have high friction. Teflon and nylon would have lower friction, but they have poor mechanical rigidity.

In the end Acrylic was chosen as the material of the harvester. While Acrylic is not a best material by any single metric, it has the necessary properties. Wide availability and ease of machining were decisive factors for the selection of acrylic over other materials.

As the minimum diameter of harvester is defined by piezo element diameter of 34 mm, both generators are designed with 35 mm square bases. Both generators also use same mounting hole pattern for electronics - 2.75 mm holes at the corners of square.

Generator was machined using slices of laser cut acrylic and standard acrylic tubing. The process is somewhat similar to 3D-printing, as several thin layers form up the final part. The acrylic parts used in generator are shown in figure 32.

While the initial approach for building the shaft of the generator was to use lasercut rings to form the shaft, the process of lasercutting warped thinner rings and

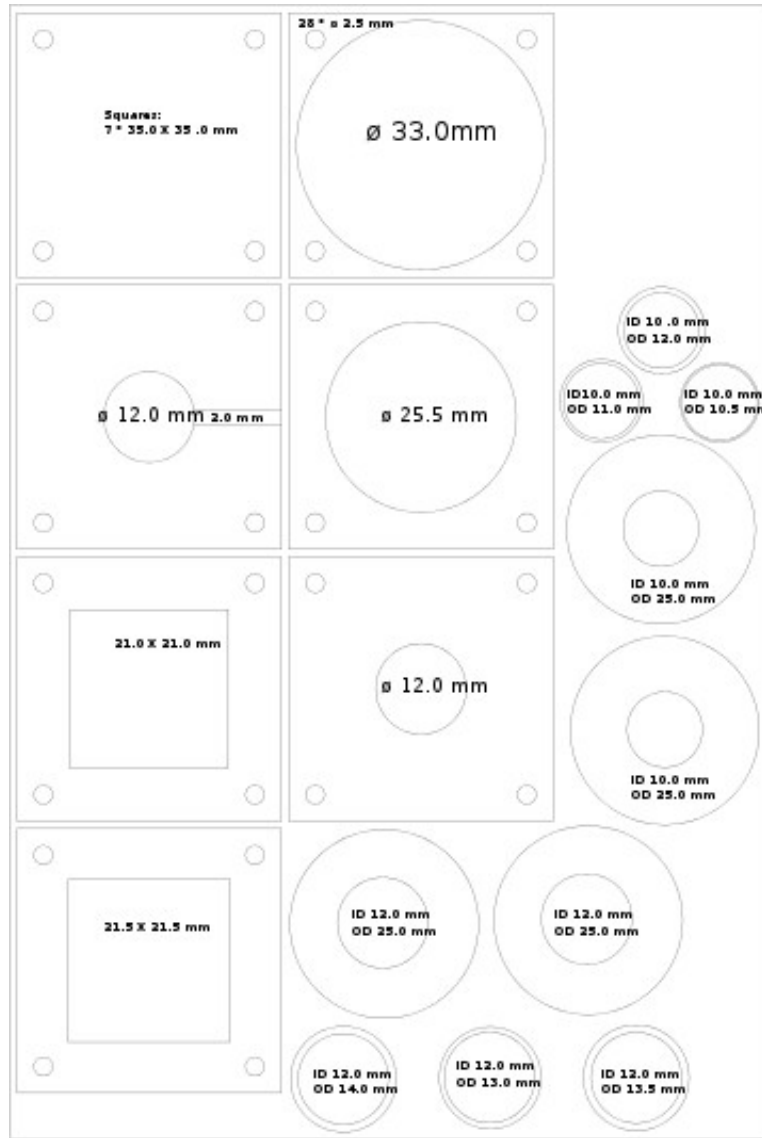


Figure 32: 150 \* 150 mm sheet for laser cut.

mechanical alignment of the rings was difficult. Therefore a standard 10 mm inner diameter 12 mm outer diameter tube was selected as the shaft.

This section detailed the material options for the harvester structure and presented the manufacturing method. Acrylic was chosen as a compromise between material properties and availability for the generator.

### 3 Results and discussion

Experimental results from harvesters are presented in this chapter. Harvesters are tested with various loads and frequencies,

#### 3.1 Experimental results of electromagnetic harvester

This section presents the experimental results from electromagnetic harvester on vibration shaker, both on resistive load and while supplying a harvester board.

The harvester was built to design presented in 2.3.4. Figure 33 shows the completed assembly. Magnet can be seen suspended in the middle, coil is formed on the upper half of generator. Magnetic spring is formed by magnets on top and bottom sides of the harvester.

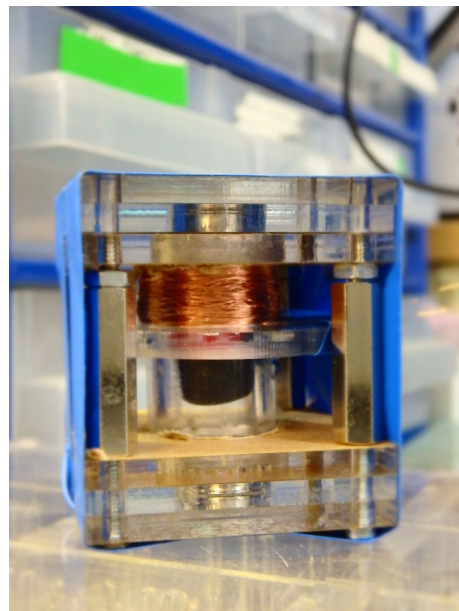


Figure 33: Finalised electromagnetic harvester.

##### 3.1.1 Test setup

This section details the test setup on vibration exciter. The electromagnetic harvester was connected to vibration exciter Brüel & Kjær type 4905 for measuring the frequency response and output power obtainable from the harvester. Figure 34 shows the test setup. Syscomp CircuitGear CGR201 oscilloscope was used to generate test signal and take the measurements from harvester. Signal from function generator was amplified by Brüel & Kjær power amplifier type 2707.

Regrettably the test setup did not have feedback for position of harvester, so exact displacement or acceleration of harvester is unknown. The output signal from function generator had amplitude of 6 volts peak-to-peak and the gain of power

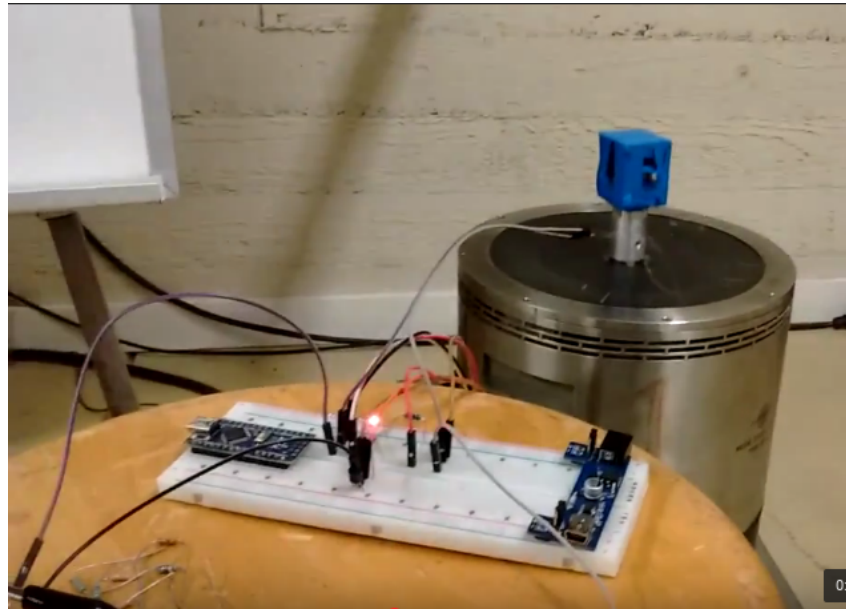


Figure 34: Test setup for harvester.

amplifier was set to 9.5 in initial testing, later the function generator amplitude was limited to 2 volts as the response was found to be identical on both settings.

### 3.1.2 Frequency domain results

One of the original design goals of the harvester was to provide a wide-band energy harvester solution. This section presents the frequency domain response of the electromagnetic harvester.

Frequency domain response was obtained by sweeping a wide-band sine signal to power amplifier and measuring the open loop response from harvester. The first measurement was done on a harvester without ferrofluid applied, figure 35 displays the measurement result. Above graph is output in decibels, below is the phase shift of the response.

There is a clear resonance peak near 70 Hz. The phase shift is almost exactly  $180^\circ$  at the resonance, which is somewhat curious result as the time domain results and theory predicted the voltage would peak at  $90^\circ$  phase when the acceleration is at zero and speed is at highest.

Amplitude does not have any specific meaning outside the context of this measurement and comparing output at different frequencies. It can be seen that original design goal of wide band response has not been achieved very well, as the amplitude response rolls off sharply below the effective frequency and maybe 20 dB / decade on frequencies above the peak. There is another resonance peak near 900 Hz, but this frequency is far above frequencies of interest for the application.

Ferrofluid was applied to rotor magnet in attempt to reduce the effect of friction, and bode diagram was similarly plotted to figure 36.

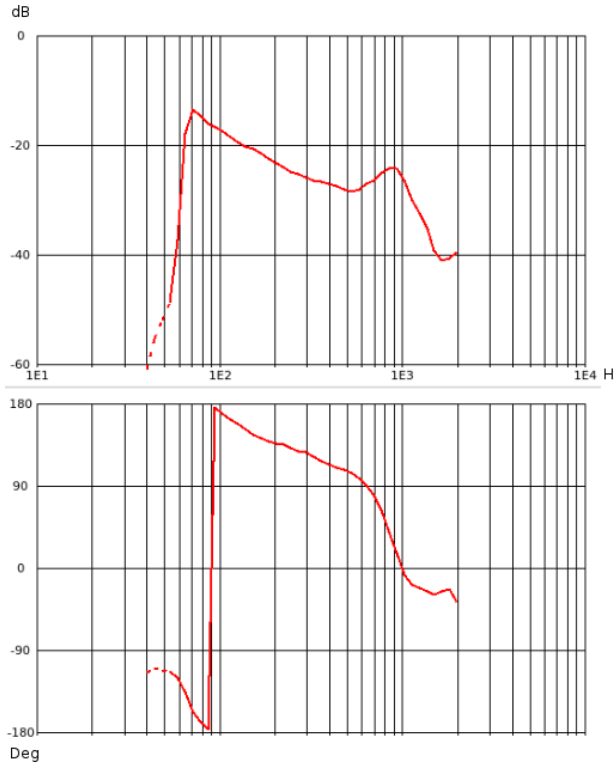


Figure 35: Frequency domain response of electromagnetic harvester before application of ferrofluid.

The application of ferrofluid shows a strong resonance peak near 70 Hz, phase shift behaviour is similar to non-lubricated experiment. Usually the systems which have second order dynamics - such as the mass damper spring system - exhibit resonance peaks when dampening factor is low. It is therefore obvious that application of ferrofluid has resulted in lesser frictional losses. Amplitude response is also at higher level across all frequencies, suggesting a better overall performance.

### 3.1.3 Time domain results

First test on the electromagnetic harvester was to measure the time domain waveforms on various loads and frequencies. After the open loop results were obtained the tests were run again with different resistive loads to measure the power output. Finally the power output to rectifier of harvesting circuit of was measured. This section presents the test results.

The magnet inside harvester had a notable amount of friction which had to be overcome before any output could be obtained from harvester. It was not possible to obtain very small signals from harvester, as any input strong enough to move the magnet resulted in volt-scale output. Figure 37 shows an example of waveforms obtained from harvester.

The waveforms presented in 37 have some curious features: the response from harvester is asymmetric, there is a notable valley of no output on the rising edge

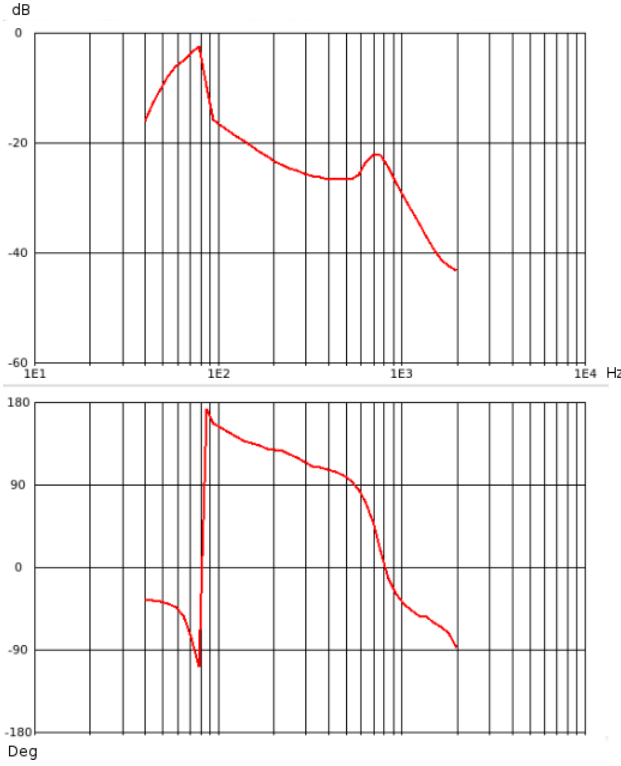


Figure 36: Frequency domain response shows a strong resonance peak after application of ferrofluid.

of the signal while no such edge is visible on falling edge. It should be noted that these valleys do not necessarily correspond to direction of gravity: the phase of input/output signal can be inversed at any point in the signal chain as the polarity of magnet, direction of winding of coils, and connection of wires can change.

There seems to be 90 °phase shift between excitation and response. This phase shift was expected, as the excitation signal drives acceleration to shaker, so speed of magnet reaches maximum at zero-crossings of excitation. This observation matches well theory presented in section 1.1.4: Voltage is proportional to rate of change of magnetic field.

Amplitude of output is 2 volts and resistance of the coil was measured to be 34 ohms at DC. Inductive component of coil impedance is negligible at the frequencies of interest, so only resistive component needs to be considered. Optimal load would then be 34 ohms. When these values are substituted in time domain into equation 6 in section 1.1.4 we obtain

$$\begin{aligned} P_{load}(t) &= V(t) * \frac{34\Omega}{34\Omega + 34\Omega} * \frac{V(t)}{34\Omega + 34\Omega} \\ P_{load}(t) &= \frac{V(t)^2}{136\Omega} \end{aligned} \quad (26)$$

Peak power would be  $\approx 30mW$ . Root mean square (RMS) voltage cannot be

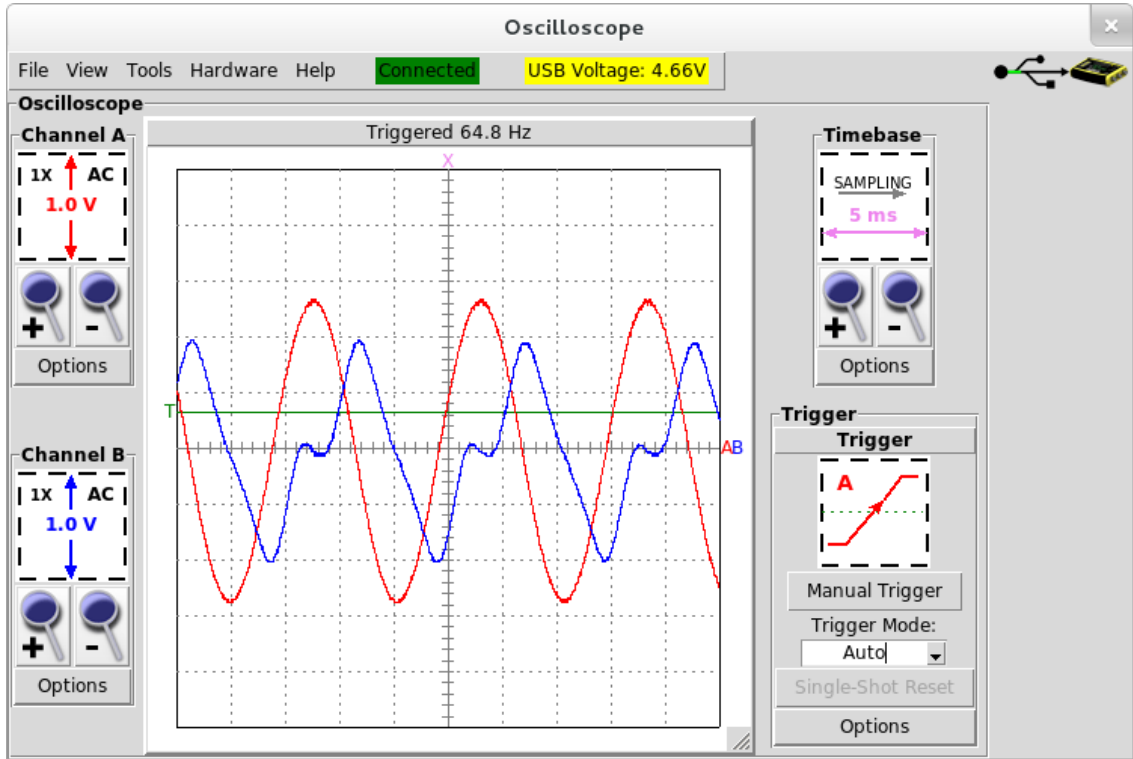


Figure 37: Open circuit response of harvester. Red is excitation waveform, blue is open-circuit voltage from harvester.

accurately calculated from given values, as the waveform is not a perfect sine or triangle wave. If the waveform is approximated as triangle wave, the RMS power would be

$$\begin{aligned}
 P_{rms} &= k * P_{peak} \\
 P_{rms} &= \frac{1}{\sqrt{3}} * P_{peak} \\
 P_{rms} &\approx 17mW
 \end{aligned} \tag{27}$$

where  $k$  is a constant multiplier for RMS power for triangle waves. If the excitation power was increased until rotor magnet audibly contacted the endstop magnets, there was no significant change in output voltage. One possible explanation is the valley in output waveform: maybe the magnet was driven to near-contact to magnet and when the acceleration was reduced the magnet was accelerated by mainly by magnetic interaction. The end result would be that the length of the valley in output waveform would vary while the output amplitude would be limited by magnetic interaction. While further exploration of this phenomenon would be interesting, the testing would be potentially destructive and therefore the tests were left to future work.

Regrettably this harvester cannot be used with the circuit designed in section 2.5 as the output amplitude is only 2 volts at any reasonable acceleration and frequency.

The circuit would require minimum of 4 volts to get out of undervoltage lockout, and this is not achievable even by connecting the bridge rectifier as voltage doubler as the energy harvesting input still has two diode drops which would keep the voltage below required threshold

Next test was done by connecting the harvester to a boost circuit based on TI BQ25504 [?]. BQ25504 has a boost-mode SMPS in energy harvesting input which is able to utilise input voltages down to 80 mV after startup and it can start up at roughly 330 mV. The detailed description of the circuit is given in section ??.

To measure the actual power output, a current-to-voltage converter  $\mu$ Current [?] was connected in series to harvester output. Measurement was done at scale  $1V = 1mA$ . Waveforms are shown in figure 38. It should be noted that the current channel might be saturated, as  $\mu$ Current cannot produce output higher than 1.25 V.

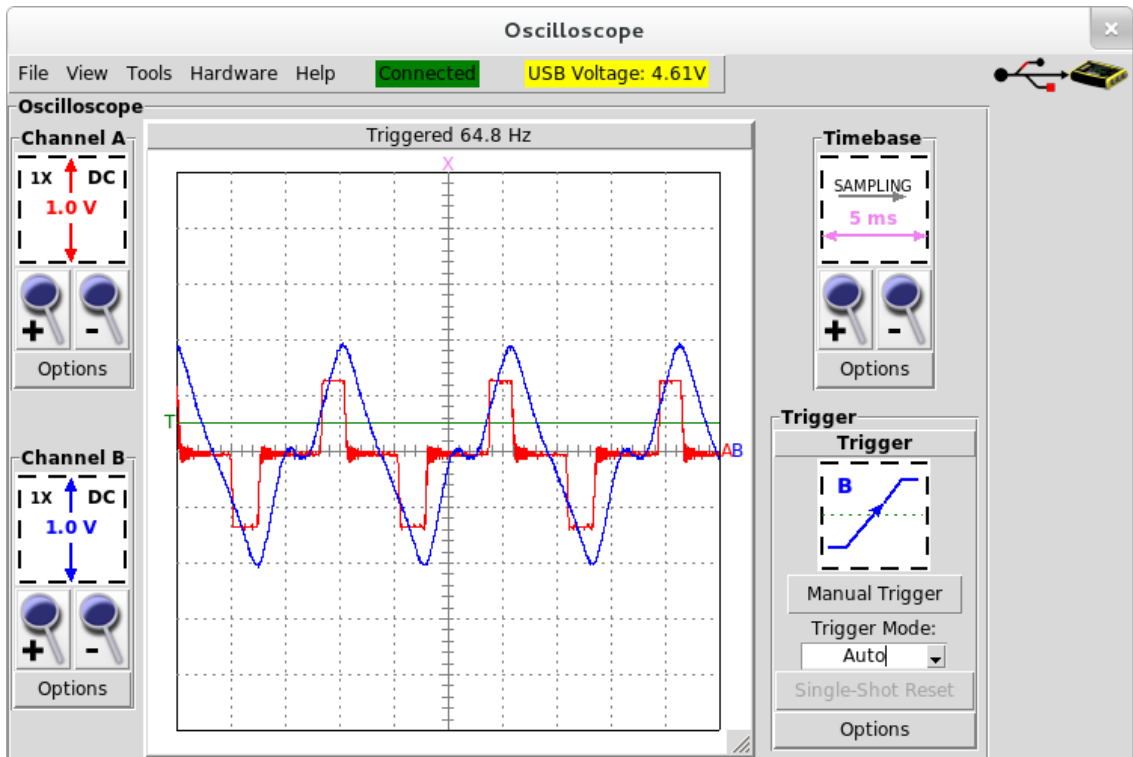


Figure 38: Voltage and current waveform from harvester. Red is current, 1 V equals 1 mA. Blue is voltage from the terminals of harvester before rectification.

The waveforms are as expected, there is no current flowing while voltage is low. When the voltage rises to roughly one volt, current starts to flow charging the output capacitor. When input voltage starts to decrease, no more current flows to capacitor. Accuracy of amplitude of current measurement is questionable because of potential saturation of measuring instrument.

It is worth noting that the voltage rises to open-loop maximum amplitude of 2 V as the loading on harvester decreases as the voltage on capacitor increases. This indicates that maximum theoretical peak power output of  $\approx 30$  mW is not reached

at any point.

Power waveform of harvester is presented in figure 39. The waveform is calculated by multiplying the voltage and current. Because current is scaled at 1 mA = 1 V, the result can be read as 1 V = 1 mW. While absolute value of power is questionable because of potentially saturated instrument, the waveform itself is correct.

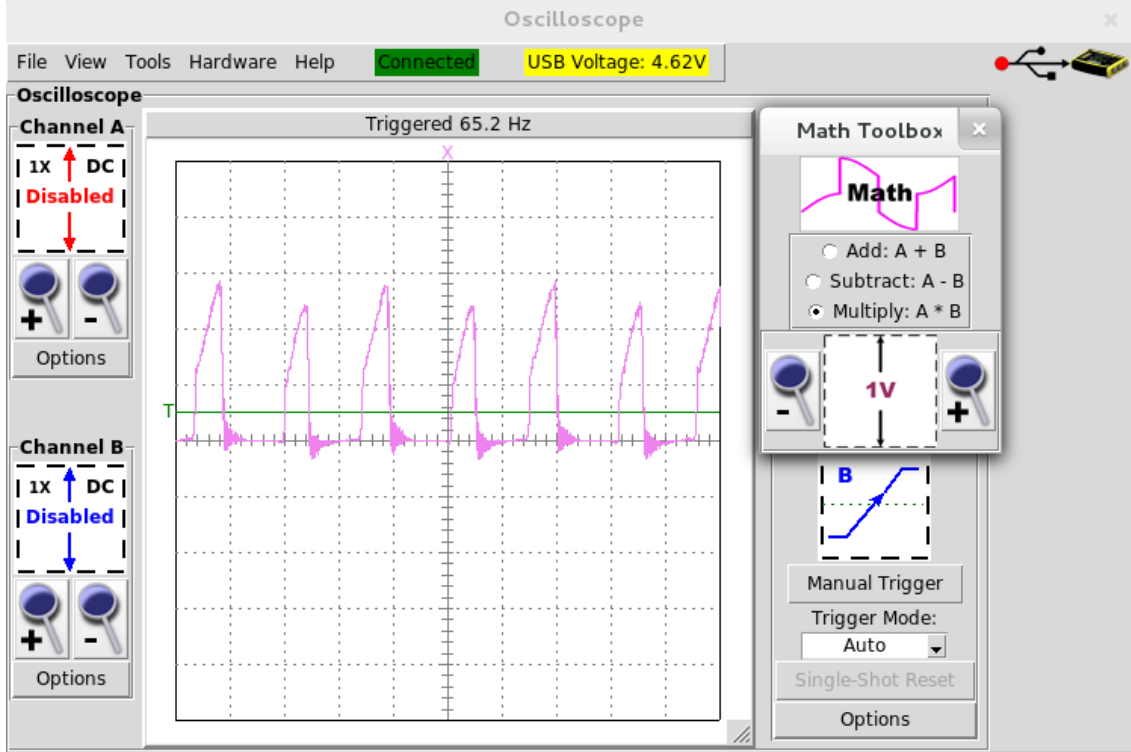


Figure 39: Power waveform from harvester. Pink is power, 1 V equals 1 mW.

Graphically read average power output is 0.375 mW. One possible reason for the greatly lesser power output was the capacitors in voltage doubler structure: the voltage doubler has series capacitance of 10  $\mu\text{F}$ , which has reactive impedance of

$$\begin{aligned} X_c &= \frac{1}{2\pi f C} \\ X_c &= \frac{1}{2\pi 6510\mu} \\ X_c &\approx 245\Omega \end{aligned} \tag{28}$$

at 65 Hz. Total output impedance of circuit would be approximately  $280\Omega$ , which would limit the output current to approximately 7 mA. This theory was tested by simulating the equivalent model of input section of harvester circuit. Simulation model and results are shown in figure ??

The simulated data confirms the effect of input capacitor to current output of system. Current is limited to roughly 7 mA. Simulated power output was on average

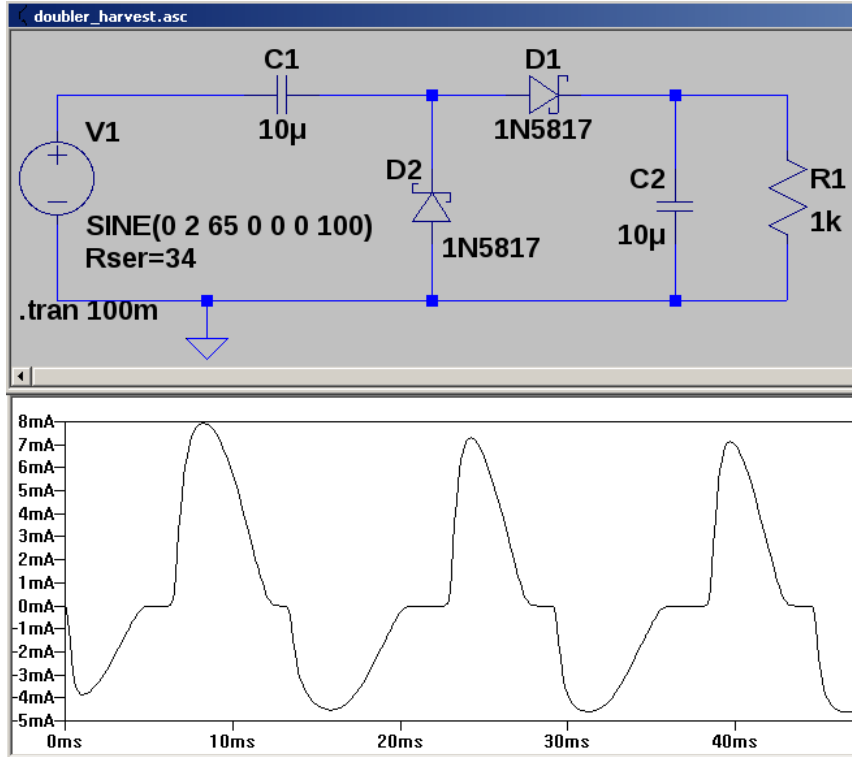


Figure 40: LTSpice model of energy harvester input section.

2.0 mW. If the measured current is assumed to be limited by saturation, and if we assume that simulated current of 8 mA peaks would be correct, the calculated power output from experimental result would be

$$\begin{aligned}
 P_{true} &= P_{simulated} * \frac{I_{simulated}}{I_{real}} \\
 P_{true} &= 0.375 * \frac{7}{1.25} \\
 P_{true} &= 2.1mW.
 \end{aligned} \tag{29}$$

After correcting the experimental current with simulated value, a lot more reasonable value of approximately 2 mW of generated power is obtained.

This section presented the time-domain results of the electromagnetic harvester on a shaker test platform. Approximately 30 mW peak power was obtained, RMS power of 17 mW was achieved to resistive load and power output to harvester was determined to be in range between 0.4 mW and 2 mW. Next section presents the frequency domain measurements of the generator as well as studies the effect of application of ferrofluid to harvester.

## 3.2 Experimental results of piezoelectric harvester

### 3.2.1 Frequency domain results

The frequency domain response of piezoelectric harvester was obtained in similar manner as with the electromagnetic harvester detailed in section 3.1.2. The excitation signal was swept across a wide spectrum and output from harvester was measured. Frequency domain results are presented in this section.

The frequency sweep result on open circuit is shown in figure ???. A resonance peak can be found at 334 Hz. Similarly to electromagnetic harvester, the slope is a lot steeper on frequencies above the resonance peak than below.

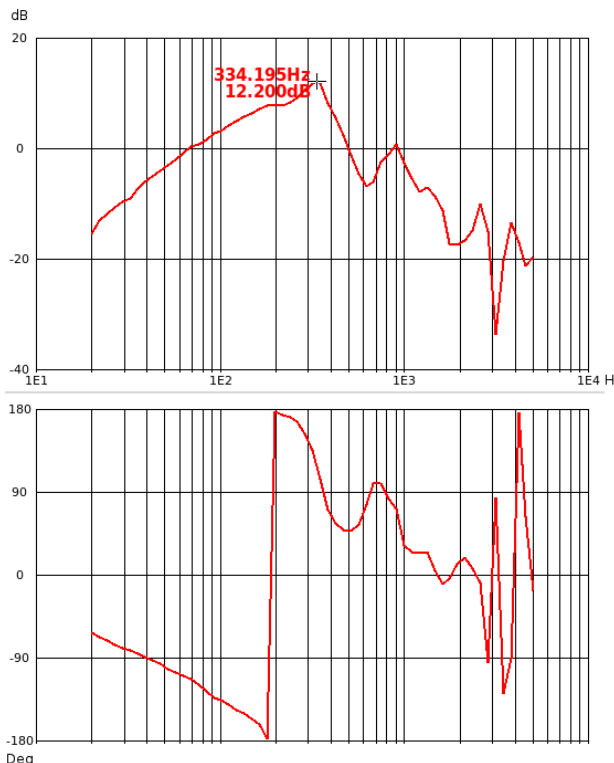


Figure 41: Frequency response of piezoelectric harvester

The peak frequency is somewhat poorly suited to environment in tyre presented in section 1.3, as the peak response is significantly above peak frequencies encountered in tyre. Usually the frequency is tuned downwards by adding mass to harvester, however this approach is not feasible in this application as the proof mass is limited to avoid damage to piezoelement due to excessive strain. However the design goal of broad band frequency response was better reached by this design.

As the peak frequency was identified near 330 Hz, the time domain analysis were performed on the harvester. Next section details the voltage, current and power outputs into varied loads.

### 3.2.2 Time domain results

This section presents the time-domain results of the piezoelectric harvester. The test setup of piezoelectric harvester was similar to the test setup of electromagnetic harvester, details of the test setup are given in section 3.1.1. Unlike electromagnetic harvester, this piezoelectric harvester did not have any obvious minimum acceleration before friction would be overcome and therefore even very small signal was obtainable. Likewise no maximum value for output signal was found by increasing the power to vibration exciter. The function generator output signal was held at 6 volts peak-to-peak for time domain tests and at 3 volts peak-to-peak for frequency domain tests to limit the loosening of screws by vibration.

The piezoelectric harvester was characterised by high output voltages at high output impedance. Open loop response is shown in figure 42. The output was not a clean sine-resembling signal as with electromagnetic harvester, it has sharp downwards peaks and a lot of high-frequency distortion.

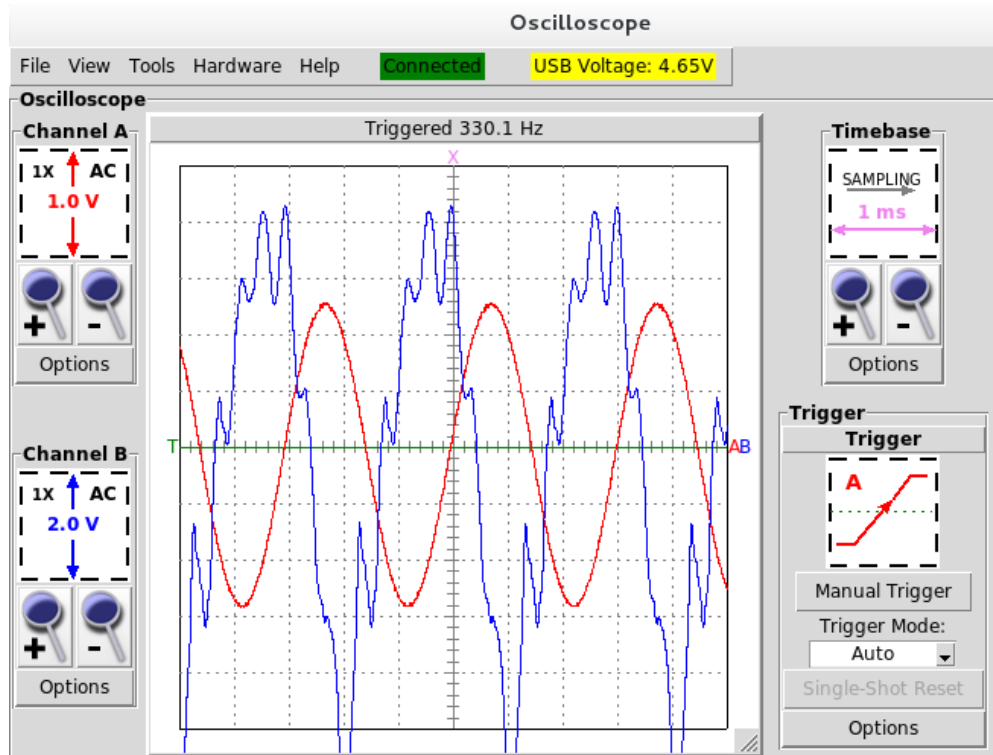


Figure 42: Open loop response from piezoelectric harvester. Red is excitation signal, blue is response.

While output signal is off the scale, negative peaks were measured at -12 volts. Peak-to-peak amplitude was therefore roughly 20 volts. The search for maximum power point was started by modeling circuit as RC- high pass filter shown in figure 43 with piezo capacitance as the series capacitor and load as the resistor.

The frequency domain results presented in section 3.2.1 were used to find the

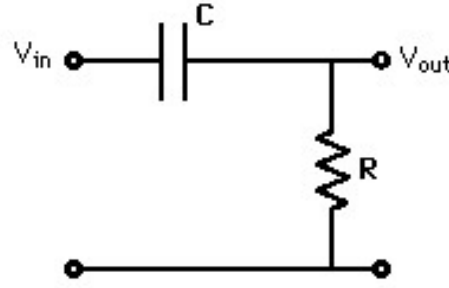


Figure 43: RC high pass filter [48].

maximum output frequency at 330 Hz. This frequency was taken as the target cut-off frequency for the RC-filter equation:

$$\begin{aligned}
 F_c &= \frac{1}{2\pi RC} \\
 R &= \frac{1}{2\pi CF} \\
 R &= \frac{1}{2\pi 39nF 330Hz} \\
 R &\approx 12400\Omega
 \end{aligned} \tag{30}$$

Theory would predict the maximum power point to be near the cut-off frequency, so the generator was tested with 18k, 12k and 9k ohm resistive loads. The peak voltages and calculated power into load are presented in table 4. The power is calculated by approximating the waveform as a clean sine calculating RMS power from peak voltage values. Method is similar to equation (27) presented in section 3.1.3, but the multiplier  $k$  is  $\sqrt{2}$  instead of  $\sqrt{3}$  as the waveform is approximated as sine rather than triangle. While the absolute value of power output suffers from approximation error, the waveforms obtained with 18 k $\Omega$  and 12 k $\Omega$  are similar enough for comparing the outputs between loads. On 9 k $\Omega$  load the waveform was clearly more distorted, and therefore the output was notably smaller than calculated.

Table 4: Output power of piezo harvester at 18 k $\Omega$ , 12 k $\Omega$  and 9 k $\Omega$  loads.

Load	Amplitude	Power <sub>rms</sub>
18k $\Omega$	7 volts	1.36 mW
12k $\Omega$	6 volts	1.50 mW
9k $\Omega$	4 volts	0.89 mW

The waveforms from 12 k $\Omega$  load and 9 k $\Omega$  load are shown in figures 44 and 45 for comparing the amount of distortion. While both waveforms show a clear

high-frequency content, possibly caused by resonant frequency of piezo element itself, the heavier loading causes a significant distortion on the waveform.

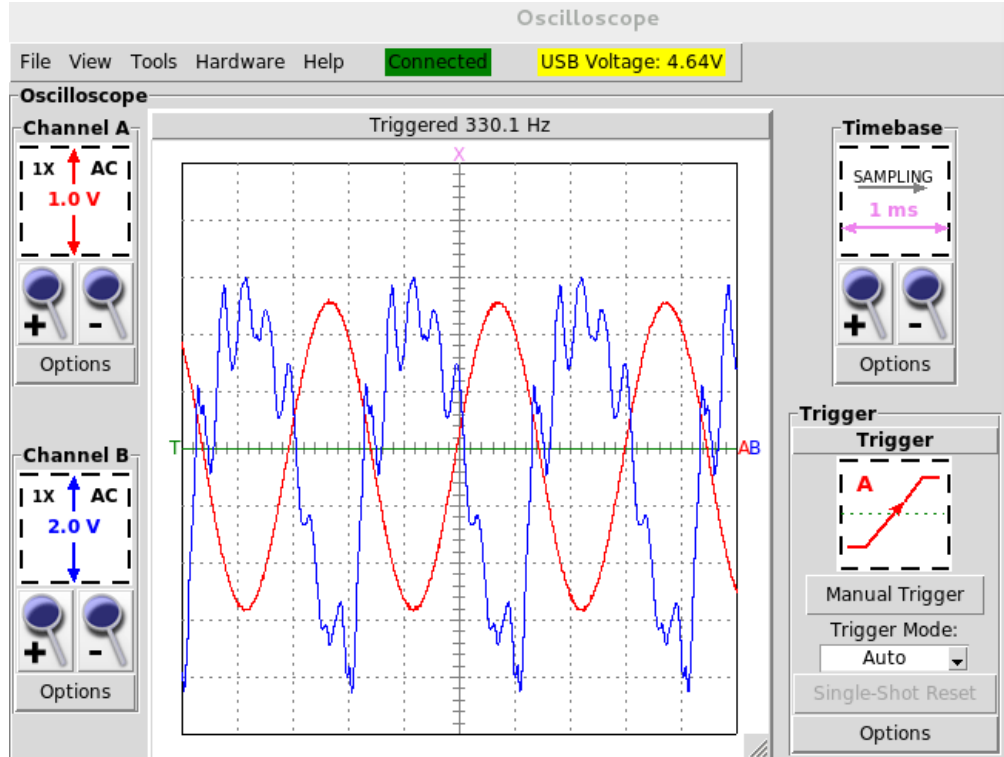


Figure 44: Piezoelectric harvester under  $12 \text{ k}\Omega$  load. Red is excitation signal, blue is response.

The waveform on figure 45 resembles almost a saw-tooth wave. Regardless of actual RMS value, it can be confidently said that the power output is smaller under  $9 \text{ k}\Omega$  load than under  $12 \text{ k}\Omega$  load. Therefore maximum power point can be concluded to be near  $12 \text{ k}\Omega$  load at 330 Hz.

After testing behaviour on resistive loads, power output to harvester through rectification was tested. While the electromagnetic harvester had notably higher output to resistive load, rectification drops voltage and therefore high-voltage characteristic of piezoelectric harvester is advantageous for rectification.

As with the electromagnetic harvester, current was measured using  $\mu\text{Current}$  at  $1 \text{ mV} / \mu\text{A}$  setting. While electromagnetic harvester suffered from reactance of series capacitance limiting the output of harvester, output impedance of piezoelectric harvester is a lot higher than that of additional series capacitor and therefore output was not impaired by coupling capacitance. The VI-waveforms are shown in figure 47.

Output of piezoelectric harvester does not follow the excitation in a similar manner to electromagnetic harvester. The output voltage is clamped by diodes of rectification circuit, and the current waveform does not follow the voltage waveform. Power output waveforms have been presented in figure ???. As before, the output can be read as  $1 \text{ V} \bar{1} \text{ mW}$ .

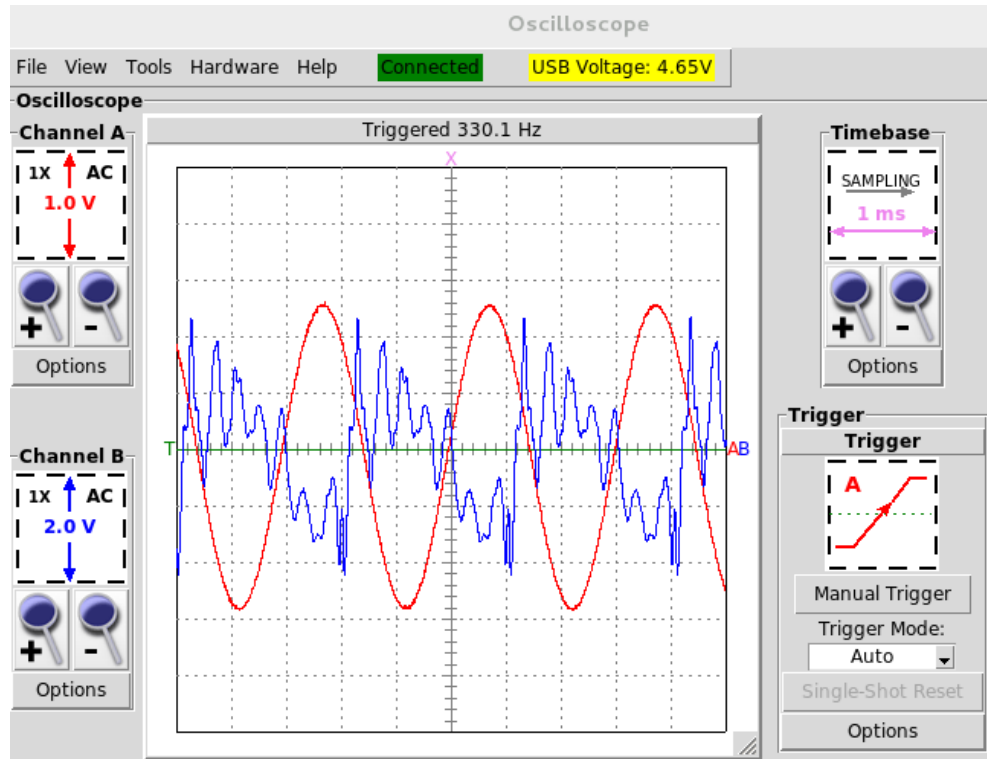


Figure 45: Piezoelectric harvester under  $9\text{ k}\Omega$  load. Red is excitation signal, blue is response.

While excitation frequency of 330 Hz was not clearly visible in VI-waveforms, the rectified signal is clearly double of 330 Hz. Graphic integration suggests the power output to be in order of hundreds of microwatts, with peak power output being approximately 2.4 mW.

It can be concluded that piezoelectric harvester produces most of the power at excitation frequency, any output from internal resonances are negligible in comparison to energy obtained from external actuation.

### 3.3 Harvesting circuit results

#### 3.3.1 Revisited circuit design

While the original idea was to use the circuit presented in section 2.5 for testing the system-level performance, it became obvious that the harvesters cannot produce output levels required by the circuit. A new simplified harvesting circuit was designed to test the performance of harvester inside tyre. The harvester design is presented in this section.

M. Rouvala kindly provided an interview [?] to discuss the energy harvesting circuitry for low-output levels. According to him, best way to utilise low output levels is to chain voltage multiplier circuit stages to produce higher DC-level and then use a boost circuit to bring the harvested output into desired level.

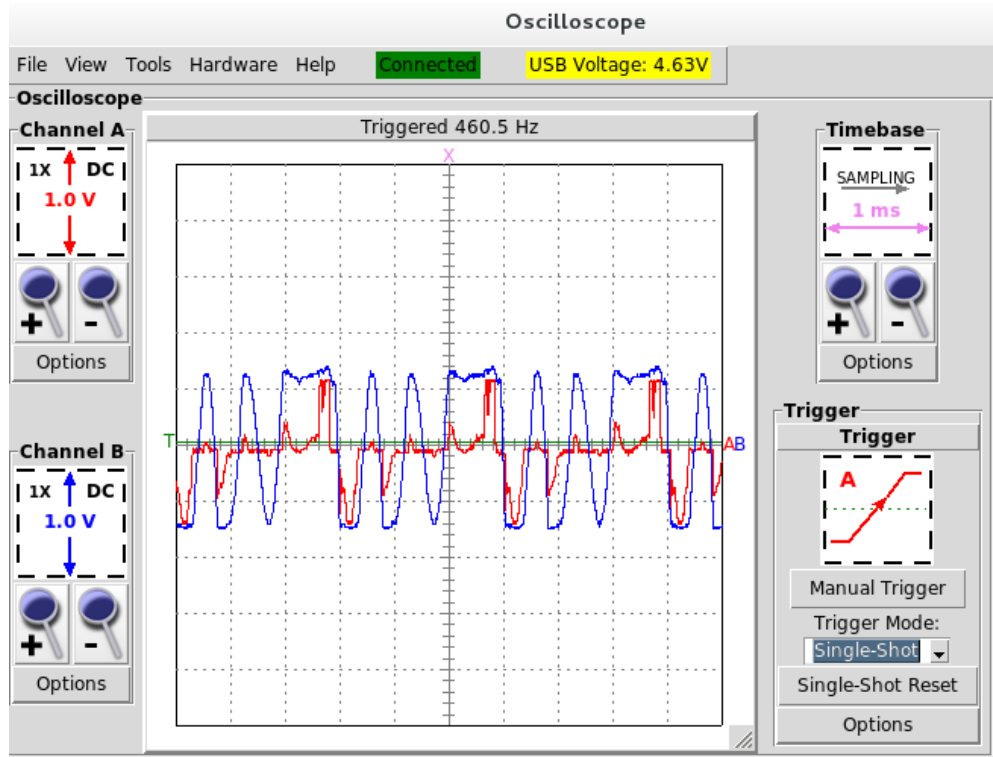


Figure 46: VI-waveforms of piezoelectric harvester into rectifier. Blue is voltage, red is current with scaling of 1 mA / V.

A few ICs from different manufacturers were considered for the new circuit, namely Seiko S-882z [?] charge pumps, Linear Technology LTC3105 [?] boost charger and Texas Instruments BQ255xx -series boost chargers. As Seiko ICs are poorly available and LTC3105 requires high start-up currents, BQ25504 [?] was chosen as the core for harvesting circuit. The schematic of harvesting circuit is presented in figure 48 and figure 49 shows the assembled circuit mounted on top of piezoelectric harvester.

The revised harvesting circuit is able to start at 0.33 V input DC voltage, or at near 0.4 V RMS amplitude AC voltage contrasted to 5 V DC level of LTC3331-based circuit. Supercapacitor was chosen as energy storage for easy measurement of accumulated harvested energy. The supercapacitor was model EECRG0V155VN [?] with 3.6 volts maximum voltage and 1.5 farad nominal capacitance.

Maximum power point tracking is provided by sampling open-loop voltage of circuit through voltage divider R1 and R2 every 16 seconds into capacitor C2. After the sample has been stored into capacitor, BQ25504 attempts to set the current taken from input so that  $V_{IN}$  matches  $V_{REF}$ .

Regrettably this form of MPPT is not adjustable by external microcontroller: while digital potentiometers exist, their current consumption far exceeds the low-power requirements of the circuit. Therefore a fixed ratio had to be set for the circuit. The ratio was set to 80 % to avoid overloading the piezo element, as it was previously

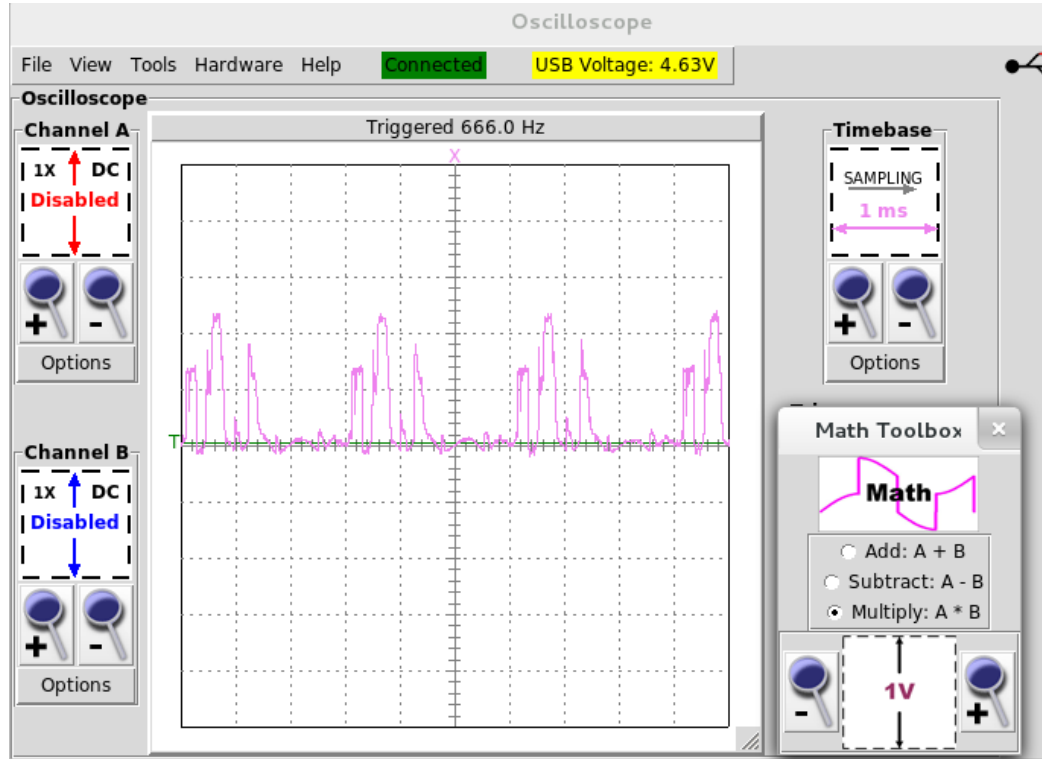


Figure 47: Power waveform of piezoelectric harvester. Scaling is 1 mW / V.

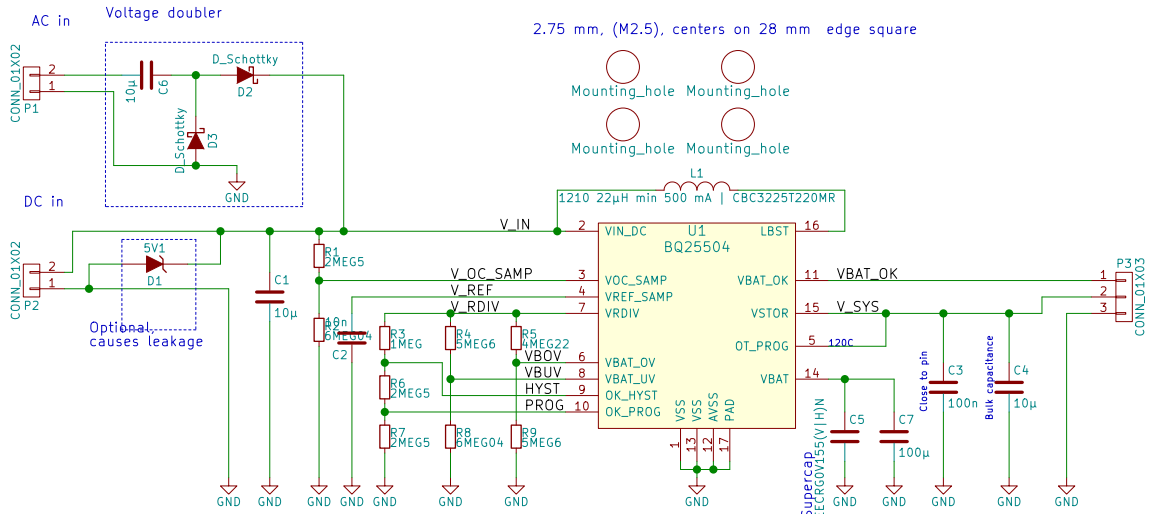


Figure 48: Schematic of revised harvester circuit

found in section ?? that overloading the element has a disastrous effect on efficiency of piezoelectric harvesting whereas underloading has much less pronounced effect on efficiency.

Resistors R3 through R9 set various operation points for the circuit. Output voltage was set to 3.3 volts, and power good -threshold was set to 3 volts on charging

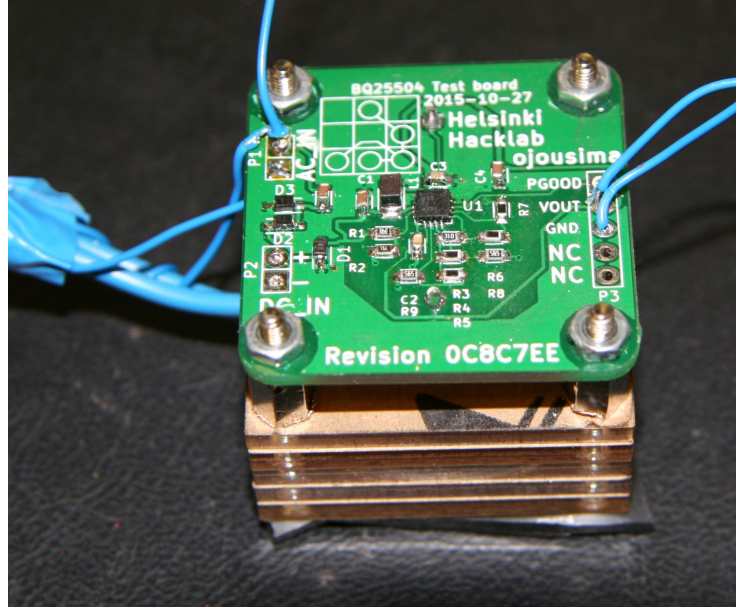


Figure 49: BQ25504-based harvesting circuit mounted on piezoelectric harvester.

and 2.2 volts on discharging.

The circuit was built and found to work with both harvester designs on shaker testbed. As the circuit was usable, further work was carried out using this circuit. Next section details the measurement of supercapacitor parameters after it was soldered in circuit.

### 3.3.2 Measuring supercapacitor parameters

As the energy storage used in circuit is a supercapacitor and all subsequent measurements are based on values measured from capacitor, the supercapacitor was characterised in-circuit to obtain more accurate values for system performance. The measuring process and results are presented in this section.

Application note AN1005 from Cap-XX [?] details a simple process for measuring supercapacitor capacitance and Equivalent Series Resistance (ESR). The supercapacitor is first charged to target voltage and then discharged through a resistor. The parameters are then read from discharge waveform. A 100 ohm resistor was used as discharging resistance, discharge waveform is shown in figure 50.

The initial discharge current can be calculated with voltage over resistor:

$$\begin{aligned} I &= \frac{V}{R} \\ I &= \frac{2.75V}{100\Omega} \\ I &\approx 27.5mA \end{aligned} \tag{31}$$

With the initial discharge current and voltage drop known, ESR can be calculated:

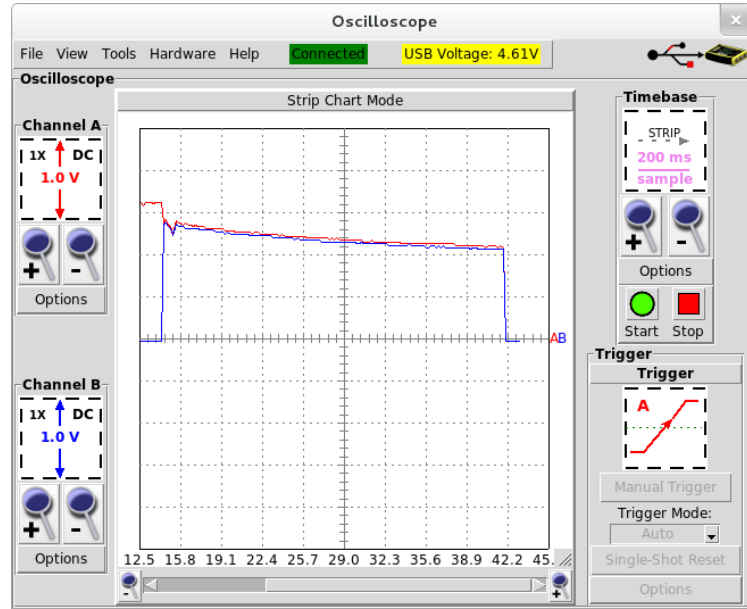


Figure 50: Discharge waveform. Red is the capacitor voltage, blue is voltage over 100 ohm resistor.

$$\begin{aligned}
 ESR &= \frac{V_{initial} - V_{discharge}}{I_{discharge}} \\
 ESR &= \frac{3.25V - 2.75V}{27.5mA} \\
 ESR &\approx 18.2\Omega
 \end{aligned} \tag{32}$$

With ESR known, it is possible to calculate capacitance from discharge time:

$$\begin{aligned}
 V_t &= V_0 e^{-t/RC} \\
 \frac{V_t}{V_0} &= e^{-t/RC} \\
 \ln\left(\frac{V_t}{V_0}\right) &= \frac{-t}{RC} \\
 C &= \frac{-t}{R} \frac{1}{\ln\left(\frac{V_t}{V_0}\right)} \\
 C &= \frac{41.6 - 14.4}{100 + 18.2} \frac{1}{\ln\left(\frac{2.75V}{3.25V}\right)} \\
 C &\approx 1.38F
 \end{aligned} \tag{33}$$

Therefore the capacitor ESR was found to be 18.2 ohms and capacitance 1.37 farads. This is well within the published initial values of ESR < 30 ohms and

capacitance of 1.5 farad -20 % ... + 80 %, and therefore results can be considered reliable.

As the devices were proven in a laboratory setting, further test was carried out to determine the power output in simulated drive inside tyre. The test setup and results are detailed in next section.

### 3.4 Performance inside tyre

The final experiment was to install the harvester with electronics inside tyre and simulate driving conditions with dynamometer platform. The test results are presented in this section.

The harvester was glued to inner lining of tyre as shown in figure 51 and electrical connections were brought through a slip ring for instrumentation. The tyre was installed to test platform presented in figure 52 and tyre was driven at varied speeds and loads.

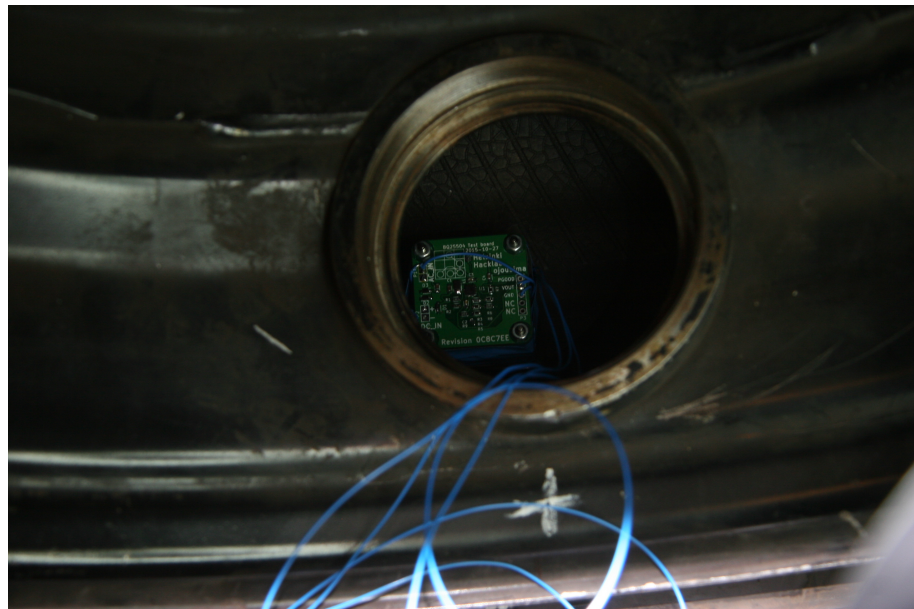


Figure 51: Harvester mounted inside tyre.

The supercapacitor was initially fully discharged. To measure boost circuit efficiency, the storage capacitor was externally charged to 3 volts and before taking measurements. Tyre was driven at varied speeds and loads. Power output was measured by recording stored voltage in supercapacitor before and after the test with NI 9215 [49].

Regrettably the device broke down during measurement at 30 km / h and therefore no accurate data was obtained. However, the results suggest that average power of 50  $\mu$ W was obtained from harvester at 30 km / h speed.

The harvesting circuit has considerable leakage of power, this is probably because of leakage characteristics of supercapacitor shown in figure 53. Initial leakage current

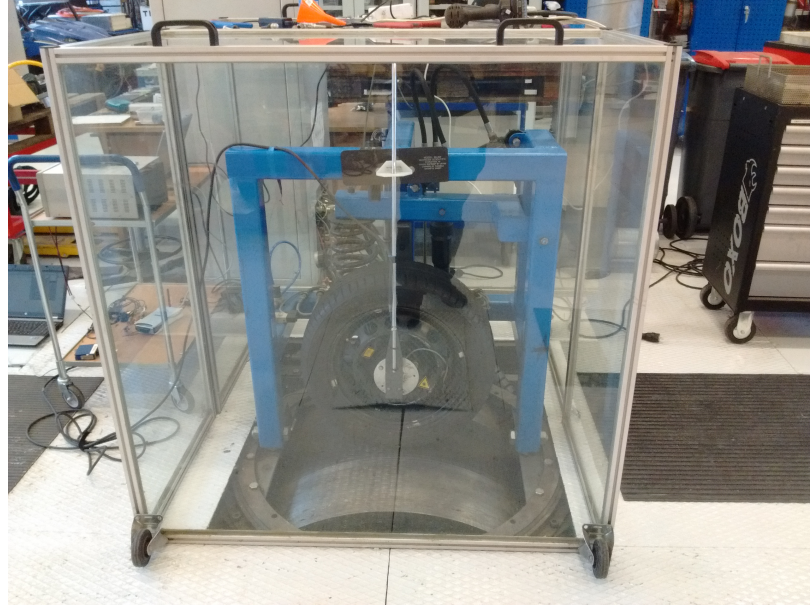


Figure 52: Tyre assembled in test platform.

Table 5: Measured values from tyre test setup.

<b>Speed</b>	<b>Load</b>	<b>V<sub>0</sub></b>	<b>V<sub>end</sub></b>	<b>Duration</b>	<b>Power</b>
0 km / h	2 kN	2.989 V	2.978 V	600 s	-75 $\mu$ W
20 km / h	2 kN	2.674 V	2.676 V	600 s	-34 $\mu$ W

of supercapacitor can be in order of tens of microamperes, and it will decrease over course of several days to specified value.

While leakage in harvester resulted in net negative power in the testing, it can be seen that harvester produced approximately 40  $\mu$ W during 20 km / h drive at 2 kN load.

This section presented the real-world power output of piezoelectric harvester. Usable, rectified and regulated power output was 40  $\mu$ W. Next section compares the obtained results to current state-of-the-art.

### 3.5 Comparison to state-of-art results

The results obtained from completed devices are compared to state of the art in this section.

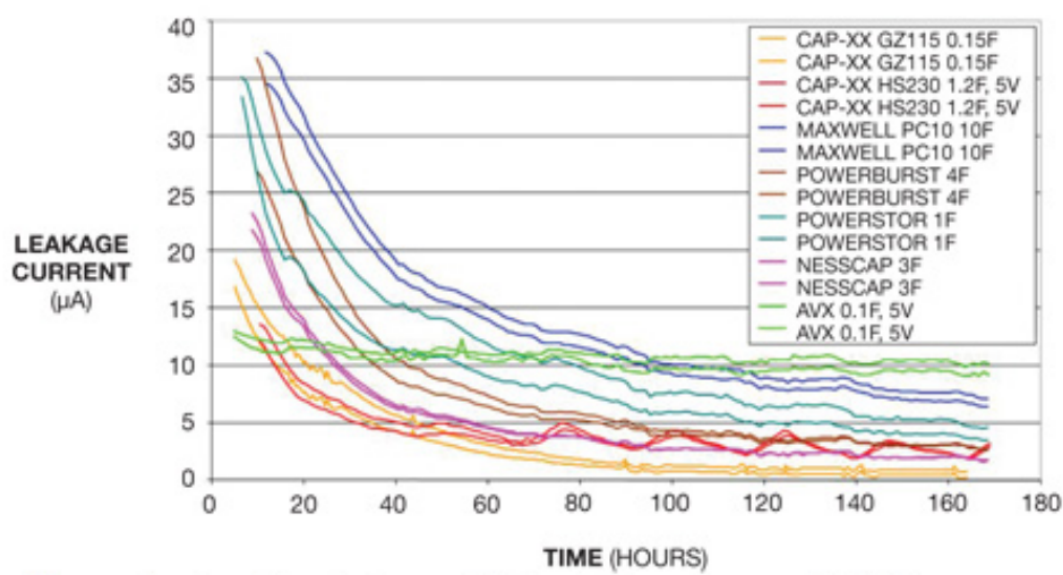


Figure 53: Supercapacitors have high initial leakage [50].

## 4 Conclusions

In this paper the operation environment of tyre has been presented, and reasonable choices for energy harvesting technology have been identified. Both Piezoelectric and electromagnetic methods have been experimented with. Electromagnetic harvester had a characteristic of low output voltage with low output impedance, and piezoelectric harvester had notably higher output voltage but also a lot higher output impedance. A boost circuit with MPPT was built to further experiment applicability of harvester in tyre environment.

The idea of applying ferrofluid to small-scale electromagnetic harvester to reduce effects of friction on magnet is novel and not presented in literature to the authors best knowledge. However, the approach has been used in larger scale energy generation and wave energy harvesting.

The piezoelectric harvester produced approximately 50 microwatts of power inside tyre at 30 km/h driving speed. The harvesting circuit failed mechanically after approximately half an hour of driving, outlining the importance of mechanical structure of device. A conference paper of these early results has been written and sent for peer review, more experiments will be performed at various speeds and loads for better characterization of system performance. The method of determining average power production from harvester using change of charge in supercapacitor is likewise original approach, most of the literature presents the power output as a function of voltage over resistive load.

As the power consumption of modern TPMS in order of tens of microwatts, the harvester system can be concluded to produce sufficient amount of power to supply current sensor systems. However, continuous sampling of sensors and transmission of data requires tens of milliwatts and therefore solutions presented in this thesis cannot supply power to such systems.

## References

- [1] Ali E. Kubba and Kyle Jiang. A comprehensive study on technologies of tyre monitoring systems and possible energy solutions. *Sensors (Switzerland)*, 14(6):10306–10345, 2014.
- [2] C. R. Bowen and M. H. Arafa. Energy Harvesting Technologies for Tire Pressure Monitoring Systems. *Advanced Energy Materials*, pages n/a–n/a, 2014.
- [3] Joseph a. Paradiso and Thad Starner. Energy scavenging for mobile and wireless electronics. *IEEE Pervasive Computing*, 4(1):18–27, 2005.
- [4] B Y Amit Lal and James Blanchard. The daintiest of dynamos. *IEEE Spectrum*, (September):36–41, 2004.
- [5] I. Boldea and S. a. Nasar. Linear electric actuators and generators. *IEEE Transactions on Energy Conversion*, 14(3):712–717, 1999.
- [6] S Boisseau, G Despesse, and B Ahmed Seddik. Electrostatic Conversion for Vibration Energy Harvesting. *Small-Scale Energy Harvesting*, pages 1–39, 2012.
- [7] S H Kim, S Ju, C H Ji, and S J Lee. Equivalent circuit model of an impact-based piezoelectric energy harvester. *Journal of Physics: Conference Series*, 557:012094, 2014.
- [8] Alper Erturk, Daniel J Inman, Scott L Hendricks, Michael W Hyer, and Ishwar K Puri. Electromechanical Modeling of Piezoelectric Energy Harvesters. *Health San Francisco*, 2009.
- [9] R. Amatya and R. J. Ram. Solar thermoelectric generator for micropower applications. *Journal of Electronic Materials*, 39(9):1735–1740, 2010.
- [10] Qi Zhang, Amen Agbossou, Zhihua Feng, and Mathieu Cosnier. Solar micro-energy harvesting with pyroelectric effect and wind flow. *Sensors and Actuators, A: Physical*, 168(2):335–342, 2011.
- [11] Feng Ru Fan, Zhong Qun Tian, and Zhong Lin Wang. Flexible triboelectric generator. *Nano Energy*, 1(2):328–334, 2012.
- [12] L Wang and F-G Yuan. Structural Vibration Energy Harvesting by Magnetostrictive Materials (MsM). *4th China-Japan-US Symposium on Structural Control and Monitoring*, pages 1–8, 2006.
- [13] Deep Patel, Rohan Mehta, Rhythm Patwa, Sahil Thapar, and Shivani Chopra. RF Energy Harvesting. *International Journal of Engineering Trends and Technology (IJETT)*, 16(8):382–385, 2014.
- [14] E. Arroyo, a. Badel, F. Formosa, Y. Wu, and J. Qiu. Comparison of electro-magnetic and piezoelectric vibration energy harvesters: Model and experiments. *Sensors and Actuators, A: Physical*, 183(June):148–156, 2012.

- [15] Kanwar Bharat Singh, Vishwas Bedekar, Saied Taheri, and Shashank Priya. Piezoelectric vibration energy harvesting system with an adaptive frequency tuning mechanism for intelligent tires. *Mechatronics*, 22(7):970–988, 2012.
- [16] G Manla, N.M White, and J Tudor. Harvesting energy from vehicle wheels. *Solid-State Sensors, Actuators and Microsystems Conference, 2009.*, 2009.
- [17] Kensuke Kanda, Takashi Saito, Yuki Iga, Kohei Higuchi, and Kazusuke Maenaka. Influence of parasitic capacitance on output voltage for series-connected thin-film piezoelectric devices. *Sensors (Switzerland)*, 12(12):16673–16684, 2012.
- [18] Hugh D. Young and Roger A. Freedman. *University Physics*. Pearson, 12th edition, 2008.
- [19] Panida Jirutitijaroen. EE2022 Electrical Energy Systems Lecture 10 : Electric Power Generation – an Equivalent Circuit of a Generator. 2012.
- [20] T O'Donnell, Chitta Saha, Steve Beeby, and John Tudor. Scaling effects for electromagnetic vibrational power generators. *Microsystem Technologies*, (April):26–28, 2007.
- [21] a N Gent and J D Walter. The Pneumatic Tire. *Rubber World*, (February):707, 2005.
- [22] Arto J. Niskanen and Ari J. Tuononen. Three 3-axis accelerometers fixed inside the tyre for studying contact patch deformations in wet conditions. *Vehicle System Dynamics*, 52(sup1):287–298, 2014.
- [23] M Löhndorf, T Kvisterø y, E. Westby, and E Halvorsen. Evaluation of Energy Harvesting Concepts for Tire Pressure Monitoring Systems. *International Workshops on Micro and Nanotechnology for Power Generation and Energy Conversion Applications*, pages 331–334, 2007.
- [24] Mika J Matilainen and Ari Juhani Tuononen. Intelligent Tire to Measure Contact Length in Dry Asphalt and Wet Concrete Conditions. *Avec 12*, pages 1–6, 2012.
- [25] Linear Technology. LTC3331 - Nanopower Buck-Boost DC/DC with Energy Harvesting Battery Life Extender. pages 1–32.
- [26] Bluegiga. BLE113 data sheet (v1.2). (November), 2013.
- [27] Data Sheet. Power Digital MEMS Accelerometer. pages 1–32, 2012.
- [28] Shuo Cheng and David P Arnold. A multi-pole magnetic generator with enhanced voltage output for low-frequency vibrational energy harvesting. *PowerMEMS 2008+ microEMS 2008*, pages 125–128, 2008.

- [29] S Jacob, V Ramanarayanan, R Karunanithi, C Damu, and G Jagadish. Development of a Moving Magnet Linear Motor Pressure Wave Generator for a Pulse Tube Refrigerator. m:361–370, 2011.
- [30] I. Boldea and S. a. Nasar. *Linear electric actuators and generators*, volume 14. 1999.
- [31] John C Elmes. Maximum Energy Harvesting Control for Oscillating Energy Harvesting Systems. page 84, 2005.
- [32] Djilali Amrani. Determination of Magnetic Dipole Moment of Permanent Disc Magnet with Two Different Methods. 2015.
- [33] S. Tornincasa, M. Repetto, E. Bonisoli, and F. Di Monaco. Energy harvester for vehicle tires: Nonlinear dynamics and experimental outcomes. *Journal of Intelligent Material Systems and Structures*, 23(1):3–13, 2012.
- [34] R W Fox, A T McDonald, and P J Pritchard. *Introduction to Fluid Mechanics*. 2008.
- [35] Medhat K Bahr Khalil. Estimated versus Calculated Viscous Friction Coefficient in Spool Valve Modeling. pages 1–9, 2008.
- [36] David Meeker. Finite Element Method Magnetics, Version 4.2, 2013.
- [37] K M Mossi, R P Bishop, R C Smith, and H T Banks. Evaluation Criteria for THUNDER Actuators 2 . Typical THUNDER Configurations. pages 1–6.
- [38] Linear Technology. LTSpice IV.
- [39] Jens Both. Leakage current properties of modern electrolytic capacitors.pdf. Technical report, 2001.
- [40] KiCAD, 2015.
- [41] Atmel. ATMEL 8-BIT MICROCONTROLLER WITH 4/8/16/32KBYTES IN-SYSTEM PROGRAMMABLE FLASH. 2014.
- [42] Philips Semiconductors. BSH105 N-channel enhancement mode MOS transistor. Technical report, 1998.
- [43] Texas Instruments. SN74AUP1T32. 2010.
- [44] Plastics International. Hardness Scale - Durometer Comparisons of Materials, 2015.
- [45] ETRA. TEKNISET MUOVIT, 2015.
- [46] Goodfellow. Polycarbonate (PC).
- [47] McCarr. High-Strength Lightweight Carbon Fiber.

- [48] R C Nave. Filter Circuits with Capacitors, 2012.
- [49] National Instruments. NI 9215 +- 10 V , Simultaneous Analog Input , 100 kS / s , 4 Ch Module. (866):1–10, 2014.
- [50] Pierre Mars. Coupling a supercapacitor with a small energy-harvesting source. *Edn*, pages 39–42, 2012.